EINDHOVEN UNIVERSITY OF TECHNOLOGY

Eindhoven University of Technology

MASTER

Characterization and mitigation of debris from a Sn-based EUV source

Gielissen, K.

Award date:
2005

Link to publication

Disclaimer
This document contains a student thesis (bachelor's or master's), as authored by a student at Eindhoven University of Technology. Student theses are made available in the TU/e repository upon obtaining the required degree. The grade received is not published on the document as presented in the repository. The required complexity or quality of research of student theses may vary by program, and the required minimum study period may vary in duration.

General rights
Copyright and moral rights for the publications made accessible in the public portal are retained by the authors and/or other copyright owners and it is a condition of accessing publications that users recognise and abide by the legal requirements associated with these rights.

- Users may download and print one copy of any publication from the public portal for the purpose of private study or research.
- You may not further distribute the material or use it for any profit-making activity or commercial gain

TU/e technische universiteit eindhoven

ASML

Characterization and mitigation of debris from a Sn-based EUV source

June 2005

Author: Kurt Gielissen
Supervisors: dr. J.J.A.M. van der Mullen*
dr. V.Banine**
ir. E.R.Kieft*

* Department of Applied Physics, Eindhoven University of Technology, P.O. Box 513, 5600 MB Eindhoven, The Netherlands

**ASML Netherlands B.V., De Run 6501, 5504 DR Veldhoven, The Netherlands

Abstract

Extreme ultraviolet lithography (EUVL) uses EUV radiation with a wavelength of 13.5 nm to carry out projection imaging. The EUV source is an essential part of an EUV lithography exposure tool. All EUV plasma sources, especially Sn-based plasma sources, not only generate the desired EUV radiation but also produce debris that limits the lifetime of the optics in the lithographic system. In order to increase the lifetime of these optics different mitigation schemes were presented and tested.

The debris can be classified into three different groups: micro-particles, slow atomic-ionic debris and fast ionic-atomic debris. For each type of debris the effect of the impact on the optics is different but they all result in reflection loss. The micro-particles lead to in a locally non-uniform surface coverage and the slow atomic-ionic debris will result in a uniform surface coverage while the fast ionic-atomic debris results in sputtering of and implantation into the surface.

It has been shown with Scanning Electron Microscopy images and software that is able to count the droplets according to their size that there is a large production of micro-particles, varying in size from 10 μm to about 100 nm. The speed of these droplets decreases with their size with the smallest particles having speeds up to 640 m/s. In a setup using a mitigation device for the droplets and measuring the atomic debris with a Quartz Crystal Microbalance (QCM) it has been found that 50% of the total mass of the deposited debris consists of micro-particles and 50% of atomic debris. The amount of slow atomic-ionic debris equals 5×10^{15} atoms/shot in a solid angle of 4π directly at the source. Measuring the total amount of fast ionic-atomic debris has been found to be very difficult without the use of an ion energy analyzer that deflects the ions according to their charge. Time of flight analysis of measurements with a faraday cup showed that the ion energies vary from 80 eV to about 4.5 keV.

Different mitigation schemes have been tested and proven to be successful. With the use of a rotating foil trap, it has been found that with a rotation frequency of 75 Hz the coverage of the droplets can be reduced to 10% after 5×10^{9} shots.
The concept of a reflective foil trap, where the foils are deliberately misaligned with respect to the source, has been tested for EUV reflection and droplet mitigation. It has been shown that coating a Mo-foil with Sn decreases the surface roughness to about 5 nm and increases the reflection coefficient. EUV reflection experiments with different grazing angles of incidence showed a good agreement with the theory and high reflection coefficients under small angles of incidence show promising expectations for development of a reflective foil trap.
An extended point source model has been described to model the transmission of droplets through a static foil trap structure. The model, where the origin of the droplets was fitted to a region of width of 2.5 mm, agreed extremely well with the experimental results. This shows that the reflected foil trap is able to mitigate the micro-particles. Thus it can be used as an alternative for the rotating foil trap.

Finally the suppression of slow atomic-ionic and fast ionic-atomic debris by an Ar-gas-controlled stationary foil trap was calculated using two different models. The suppression of slow atomic-ionic debris was measured with a QCM and a suppression factor of 33 was experimentally observed.

With the Anisotropic Diffusion model, the lifetime of the optics for a *pd*-value of 2 mbar $\times$ cm has been found to be equal to 10^8 shots. A cleaning strategy will be used to improve the lifetime to 5×10^9 shots. The beam extinction model showed that with a *pd*-value of 2 mbar $\times$ cm the suppression of the fast-ionic debris is about 3000.

Table of contents

Abstract **1**

Table of contents **3**

1. Introduction **5**

2. Sn-based EUV source **8**
- 2.1 Introduction 8
- 2.2 Description of the source 9
  - 2.2.1 Working principle 9
  - 2.2.2 Electrodes 10
  - 2.2.3 Laser 12
- 2.3 Discharge characteristics 13

3. Debris **15**
- 3.1 Introduction 15
- 3.2 Origin of the debris 16
  - 3.2.1 Anode/Cathode erosion 17
  - 3.2.2 Plasma plume 17
- 3.3 Micro-particles 18
  - 3.3.1 Introduction 18
  - 3.3.2 Experiments 19
- 3.4 Slow atomic-ionic debris 21
  - 3.4.1 Introduction 21
  - 3.4.2 Experiments 22
- 3.5 Fast ionic-atomic 23
  - 3.5.1 Introduction 23
  - 3.5.2 Faraday cup experiment 23

4. Mitigation **26**
- 4.1 Rotating foil trap 27
  - 4.1.1 RFT principle 27
  - 4.1.2 RFT experiments 29
    - 4.1.2.1 Experiment with the ASML Sn-source 29
    - 4.1.2.2 Experiment with the Philips Sn-source 32
- 4.2 Reflective foil trap 36
  - 4.2.1 EUV reflection experiment 36
    - 4.2.1.1 Introduction 36
    - 4.2.1.2 Experiment 37
  - 4.2.2 Particle mitigation experiment 41

4.2.2.1 Introduction 41
4.2.2.2 Experiment 45
4.3 Gas controlled stationary foil trap 47
4.3.1 Cross-section and mean free path 47
4.3.2 The gas controlled SFT principle 49
4.3.2.1 Beam extinction model ($b << \lambda$ *and* $b << L$) 51
4.3.2.2 Anisotropic diffusion model ($\lambda \approx b << L$) 52
4.3.3 Experiment 55

5. Discussion 58

6. Conclusion 63

References 65

Appendix A: Working principle of a Quartz Crystal Microbalance 68

Appendix B: Transmission of the Nb-filter 69

Appendix C: Transmission of droplets through the foil trap 70

1. Introduction

People that use electronic products and personal computers are used to the regular improvements in such systems as time passes. Every year new types of computers enter the market that are faster and offer more memory space than the previous generations. In the pursuit of ever faster and more complex computers the features on integrated circuits (IC) become smaller and smaller. According to Moore's law the number of transistors on integrated circuits doubles every year.

Lithography is a crucial step in the production of integrated circuits. In order to fulfill the demands of the costumers, the resolution of the lithography machines has to improve. However with the current Deep Ultraviolet lithography a feature resolution of 70 nm is the maximum achievable. To get a better resolution a new technique is needed: Extreme Ultraviolet Lithography (EUVL).

Although EUVL is similar to optical lithography, the reduced wavelength introduces several unique challenges. The light production systems change from conventional lamps and lasers to plasma light sources of relatively high temperature. And since various materials and gases are strongly absorbing for EUV radiation, EUVL systems require vacuum operation. In addition the optics should be reflective in nature as no material is transparent enough for EUV to make use of refractive optics.

Light source development is one of the key elements in the progress of EUVL as it moves towards becoming the technology for fabrication of the next generation microchips. The use of EUV radiation with a wavelength of 13.5 nm in comparison to the longer wavelength of UV allows reducing the width of a line-space pair to 64 nm, which is defined as the 32 nm node. The wavelength of 13.5 nm is defined by the use of a system of multilayer coated mirrors to image a reflective mask on a photoresist. Details on EUVL are found in references [1] [2].

The EUV light source has to fulfill extremely high demands, both technical and cost oriented. The EUV source is required to radiate adequate light at 13.5 nm, compatible with the narrowband Mo-Si multilayer mirrors used in the collection and imaging optics. The unusual spectral band is defined by the fact that the Mo-Si mirrors combine best high reflectivity and usable bandwidth [3]. Various technical concepts for realizing high power sources for EUVL are under investigation worldwide [2] [4] [5]. The main candidates for EUV-sources are gas discharge plasmas (DP) and laser produced plasmas (LPP). Discharge produced pinch plasmas in general are of special interest [6], because their prospected costs are expected to be much lower than with that of systems which are based on laser produced plasmas [7].

The required radiation from the EUV source lies within a 2% wavelength band around 13.5 nm. Discharge plasmas in Xe, Sn and Li are useful sources of this radiation. Li being a line-emitter, is the most sensitive to the operating wavelength and only has a linewidth

of 0.03 nm [3]. In many discharge sources, Xe is applied as the working element because it is not easily deposited on or chemically reacting with the surfaces of multilayer mirror optics. However Xe is not expected to be able to meet the power requirements from the industry. Therefore the center of attention has recently shifted towards the use of Sn as an alternative working element. Despite the obvious drawback that Sn is a solid under normal conditions, it is an interesting element because of the highly favorable shape of its spectrum in the EUV range (figure 1.1).

All plasma EUV sources, and especially Sn-based sources, not only generate the desired radiation at a wavelength of 13.5 nm but also produce debris. Since the Mo-Si multilayer mirrors, used in the collection and imaging optics are located in the line-of-sight to the EUV source, all the radiation from the source and the emitted debris can damage the mirrors; which limits the lifetime of the optics in the lithographic system.

In this study we follow the convention in which the lifetime of the EUV optical system is defined as the number of shots until the collector mirror reflection becomes worse than 10%. In order to increase the lifetime of the optics, debris mitigation is indispensable. That is the main subject of this report.

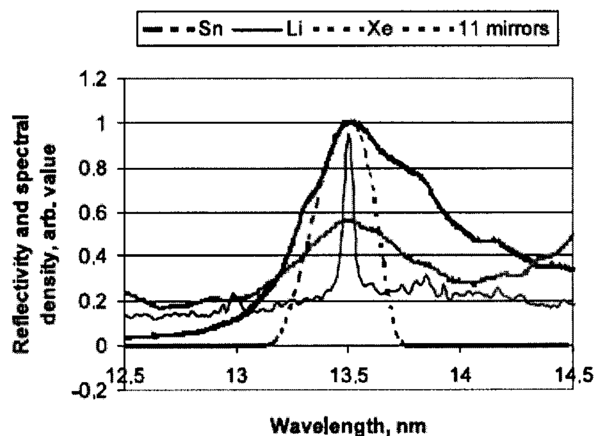

Figure 1.1 The spectra of Sn, Li and Xe together with the calculated near normal incidence reflectivity of the mirror system [3].

In general one can distinguish between three types of debris and their effect on the optics:

1. Micro-particles or particulate debris
2. Slow atomic-ionic debris
3. Fast ionic-atomic debris

For each type of debris the effect of the impact on the optics is different but they all result in reflection loss. The micro-particles will result in a locally non-uniform surface coverage and the slow atomic-ionic debris will result in a uniform surface coverage while the fast ionic-atomic debris results in sputtering of and implantation into the surface.

The different mitigation schemes include:

- A Rotating Foil Trap (RFT)
- A reflective foil trap
- An Argon gas-controlled Stationary Foil Trap (SFT)

The *RFT* is a mitigation device designed to stop the micro-particles. It is used in combination with a *SFT* to stop the micro-particles with a vertical velocity component.

The idea of the *reflective foil trap* is that it stops the micro-particles and that the EUV photons are transmitted through reflection by the foils. The foils are aligned in such a way that the transmission of EUV photons is as large as possible and that all the micro-particles will hit the foil under an angle at which the particles stick to the foil. Unlike the RFT, the reflective foil trap will mitigate the micro-particles without the need to rotate the foils. If Ar-gas is injected in the reflective foil trap it will have the same working principle as a gas controlled SFT for mitigation of the slow and fast atomic-ionic debris.
The concept of a reflective foil trap has been tested for EUV reflection and droplet mitigation. EUV reflection experiments with different grazing angles of incidence showed promising expectations for development of a reflective foil trap. A model has been described to calculate the transmission of droplets through a stationary foil trap. The model, where the origin of the droplets was fitted to a region of width of 2.5 mm, agreed extremely well with the experimental results. This shows that the reflected foil trap is able to mitigate the micro-particles so that it can be used as an alternative for the rotating foil trap.

The suppression of slow atomic-ionic and fast ionic-atomic debris by a *gas-controlled stationary foil trap* (SFT) was calculated using two different models. The suppression of slow atomic-ionic debris was measured with a Quartz Crystal Microbalance (QCM).

With the Anisotropic Diffusion model, the lifetime of the optics for a *pd*-value of 2 mbar $\times$ cm has been found to be equal to 10^8 shots. A cleaning strategy will be used to improve the lifetime to 5×10^9 shots. The beam extinction model showed that with a *pd*-value of 2 mbar $\times$ cm the suppression of the fast-ionic debris is about 3000.

This report is organized as follows. In chapter 3 we will present the results of the experiments performed to characterize the debris. The experimental results and some models concerning the debris mitigation are presented in chapter 4. Some problems encountered during the experiments and the effect of the mitigation schemes on the collector mirror lifetime are discussed in chapter 5. Finally chapter 6 presents the conclusions.

We continue with chapter 2 that provides a short description of the Sn-based EUV source, installed at the EUV laboratory of ASML in Veldhoven. The working principle and some plasma characteristics of the discharge are presented.

2. Sn-based EUV source

2.1 Introduction

A new, redesigned copy of the laser-triggered Sn discharge source from ISAN [8], seen on figure 2.1, was installed early in 2003 at the EUV laboratory of ASML in Veldhoven. The device is a discharge plasma source working on Sn vapour, designed to generate EUV radiation. It is an experimental setup with the purpose to gain knowledge on the physical properties of Sn pinch plasmas and debris generation. This chapter will give an overview of the working principle of the Sn-based EUV source, further denoted as the Sn-source. The main elements, like the electrodes and the trigger laser, required for basic operation will be described. Finally some experimental results of the discharge characteristics are presented.

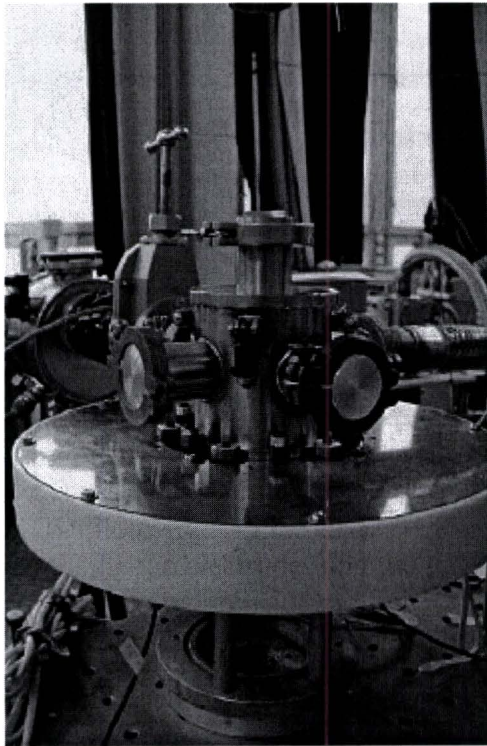

Figure 2.1 The source at the ISAN laboratory. The large circular disk is the capacitor bank and in the center, on top of the disk, the vacuum chamber can be seen. To the back right the vacuum pump is connected; to the back left an in-band EUV power meter can be seen. The laser pulse enters the vacuum chamber from the top.

2.2 Description of the source

2.2.1 Working principle

A high voltage discharge is generated in Sn vapour in an otherwise vacuum environment. This leads to the so-called pinch effect, so that plasma properties are achieved that are favorable for the generation of EUV, like high particle densities and electron temperature. The working principle of the source is shown in figure 2.2.

The discharge region consists of a flat, grounded cathode that is covered with Sn and a semicircular anode located 3 to 3.5 mm above the cathode. Before the start of the discharge a positive electrical potential of 4 kV is applied to a capacitor bank, of which the positive side is connected to the anode. The evaporation of Sn, as well as some pre-ionization is achieved by firing a laser pulse onto the Sn-covered bottom electrode surface. This creates a very localized, partially ionized Sn vapour, which expands towards the edges of the anode.

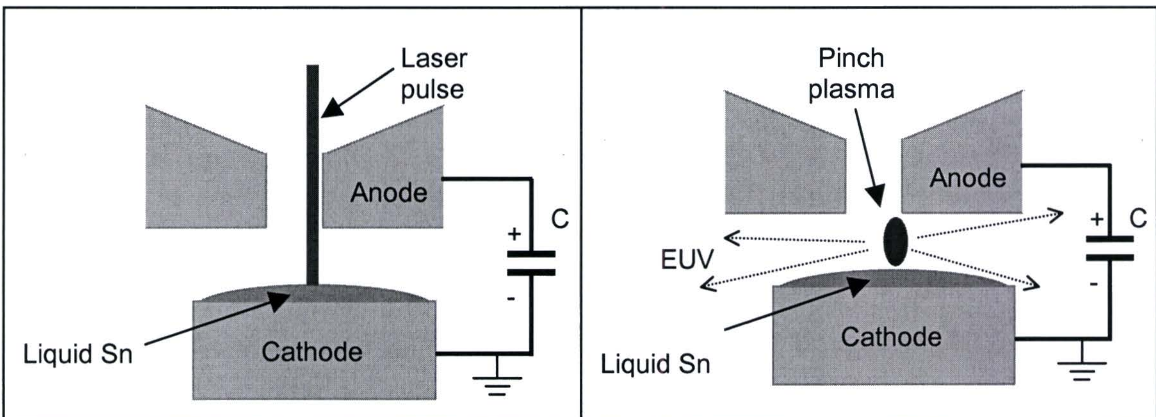

Figure 2.2 Working principle of the discharge. The cathode is covered with liquid Sn. A laser pulse is fired onto the cathode surface to evaporate the liquid Sn. The Sn-vapour expands towards the edge of the anode, which is connected to the positive side of the capacitor bank (C). Once the Sn vapour near the anode has reached a sufficiently high density a discharge is initiated. The EUV generated by the plasma can be viewed from the side.

Once the Sn vapour near the anode has reached a sufficiently high density, a discharge is initiated. The current through the discharge increases to almost 20 kA in only a few tens of ns time, and a multiply ionized, EUV emitting plasma is formed [9]. The strong current causes a pinch effect. This means that due to the Lorentz forces acting on the charged particles in the plasma, the plasma is compressed, in the radial direction, to a needlelike shape. The EUV generated by the plasma can be viewed from the side, leading

to low re-absorption of EUV, and low debris in the viewing direction, as most of the pinch material eventually expands in the axial direction.

In the next chapters, a shot will be defined as one single discharge, producing EUV radiation and debris. (10^3 discharges will be a kshot etc.)

2.2.2 Electrodes

The source is operated with its axis of symmetry in the vertical direction. The bottom electrode is a small cylindrical hollow tube filled with Sn (Sn pool), and serves as cathode. The top electrode, the anode, is a half round disk and is screwed tight with a large circular screw, which has a hole in the center to let the laser beam reach the cathode surface from the top. See figure 2.3 for a view of the electrodes in their holders. Through the opening in the anode holder, the top of the cathode and the bottom of the anode can be seen.

In order to increase the amount of evaporated material, increase stability of the discharge and keep the surface of the cathode smooth, the cathode is heated to above 300 °C. The heating occurs with a metal spiral that carries a current. The temperature of the cathode is monitored by a thermocouple, which is located at 2 mm from the bottom of the Sn pool.

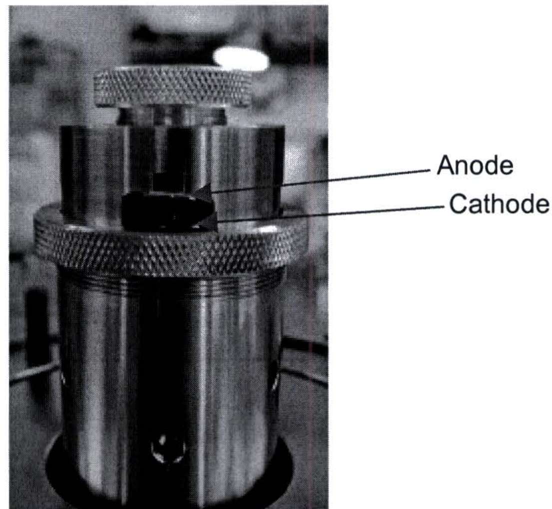

Figure 2.3 The anode holder viewed from the side, without the vacuum chamber cover present. Through the opening in the side, the electrodes (anode top, cathode bottom) can be seen.

The anode is made of molybdenum (Mo) that has a very high melting temperature and is easier to process than tungsten. Also its solubility in liquid Sn is much lower than that of stainless steel; Sn is a very aggressive solver of steel at any temperature above its melting point. Therefore the choice of Mo is because of the low erosion rate. However after a

large number of discharges the Mo-anode erodes and some material is deposited on the Sn cathode. This contaminates the cathode and increases its melting temperature. This could be observed when the cathode was cooled down after a long during experiment. The cathode surface wasn't smooth anymore and the area were the laser evaporated the Sn could be clearly seen.

During operation the cathode is at a ground potential while the anode is connected to the high voltage side of the capacitor bank. The capacitor bank consists of three groups of parallel capacitors, placed in series. Special attention was paid to avoid exposure of any parts under high voltage on the outside of the setup. All metallic parts that are on the outside of the device are on ground potential.

The high voltage side of the discharging circuit is connected to a power supply that charges the capacitor bank to a maximum voltage of 5 kV continuously. The repetition frequency of the source is determined, within the limitations of the high voltage power supply, by the repetition rate that is set for the laser. When a laser shot is fired, the capacitors in the circuit are discharged through the pinch volume. They are charged again on a longer timescale through a slower circuit that connects the power supply to the capacitor banks. When any considerable charge appears on the capacitors again, the plasma will already have died and vacuum will have been restored, so that no premature discharges can take place.

A probe has been inserted into the circuit for measuring the discharge current. The voltage from the probe is a measure for the current in the discharge circuit and can be registered directly by an external oscilloscope. Table 2.1 gives an overview of the values of some of the main parameters of the discharge circuit. The duration of one oscillation in the current characteristics is indicated by τ. The number for the repetition rate is based on the capacity of the high voltage power supply. The actual operation frequency is limited to 10 Hz due to the repetition rate of the laser.

Table 2.1 An overview of parameters of the laser-triggered Sn discharge source.[8]

Quantity	Value	Quantity	Value
C	369 nF	V_{max}	5 kV
L	4.5 nH	E	3.6 J
$\tau = 2\pi\sqrt{LC}$	260 ns	f_{max}	20 Hz

2.2.3 Laser

The laser that is used for ablation and ignition is the LT-11 from the Polys Research & Development Institute in Moscow [10]. It is a single-rod, water cooled, optoelectronically Q-switched Nd:YAG laser, with a maximum repetition rate of 10 Hz. This type of laser is used because it is easily available and cost efficient and does not require any special safety measures regarding the treatment of gases.

The laser operates in the TEM_{00} mode, at the principal wavelength of 1064 nm. The pulse duration is 10 ns. The beam diameter and divergence at the exit of the laser are about 3.8 mm and 1.5 mrad, respectively. Typical pulse energy at 1064 nm, required for a stable discharge, is around 100 mJ. A much smaller energy of a few tens of mJ is already sufficient to start a discharge, but stability is enhanced when stronger pulses are applied. The maximum pulse energy is 150 mJ. This pulse energy corresponds to a voltage on the flash lamp of 850 V. Standard operation is with a voltage between 600 and 800 V [8].

The conversion efficiency increases with increasing pulse energy but after a certain optimum value it seems to decrease somewhat. Increasing the pulse energy leads to a smaller delay between the laser pulse and the start of the discharge current. However it leads to a larger delay between the onset of the current and pinching. This can be explained by the increased amount of ablated material when a larger pulse energy is applied: first contact of the vapour with the anode will be reached faster but it will take more time to pinch the larger amount of material.

2.3 Discharge characteristics

The time development of the discharge can be roughly split into four main phases:

1. The *ignition* phase
   Caused by the firing a laser pulse onto the surface of the cathode. A plume of vaporized and partly ionized Sn expands into the vacuum until it reaches the edge of the anode.

2. The *prepinch* phase
   When a sufficiently conducting path has been created a discharge starts. The electric current heats and ionizes the Sn plasma further and the plasma starts to compress in the radial direction.

3. The *pinch* phase
   The plasma reaches a narrow, elongated shape. Due to the increase in density that is caused by the compression, the emission of EUV radiation is strongest in this phase. Because of the compression of the plasma during the pinch phase, a lot of the pinch material is pushed away in the axial direction. This ion bombardment leads to vaporization of the anode material [11] and micro-particle ejection at the liquid cathode surface [12].

4. The *decay* phase
   Because there is no confinement of the plasma in the axial direction and the limited amount of charge in the capacitor bank, the plasma starts to expand and decay until finally vacuum between the electrodes is restored.

The actual pinch phase has a duration in the order of 10 ns, and is therefore very short lived compared to the other phases of the discharge. The pinch occurs about 300 ns after the ignition of the discharge. Compression of the discharge plasma starts about 30 ns before the actual pinch. During compression, the EUV emission rapidly increases. It disappears about 40 ns after the pinch, as seen on figure 2.4.

A method that can give direct information on both electron densities and temperatures is Thomson scattering spectroscopy. In this technique, a laser pulse is fired through the plasma and the spectrum of the laser light scattered from free electrons in the plasma is recorded. The electron density can be derived from the total intensity of the scattered light. The width of the spectrum is proportional to the square root of the local electron temperature. The results on the prepinch phase of the discharge are presented in [13] [14]. Electron densities increase from 1×10^{23} m^{-3} to 1×10^{24} m^{-3} and the temperatures increase from 5 eV to over 30 eV in about 100 ns. Latest research about the discharge properties during the pinch phase shows that electron densities increase to 3×10^{25} m^{-3} [15].

Just after the pinch, visible light appears along the cathode surface. This is generated by a plasma that expands towards to anode with a speed of 5×10^4 m/s. Since a similar emission feature does not appear in the EUV, it must be generated by a much cooler plasma. Most likely, the current through the pinch plasma and absorption of EUV radiation lead to heating of the liquid Sn on the cathode surface. Evaporation and partial ionization of Sn from the cathode can result in a relatively cool plasma [9].

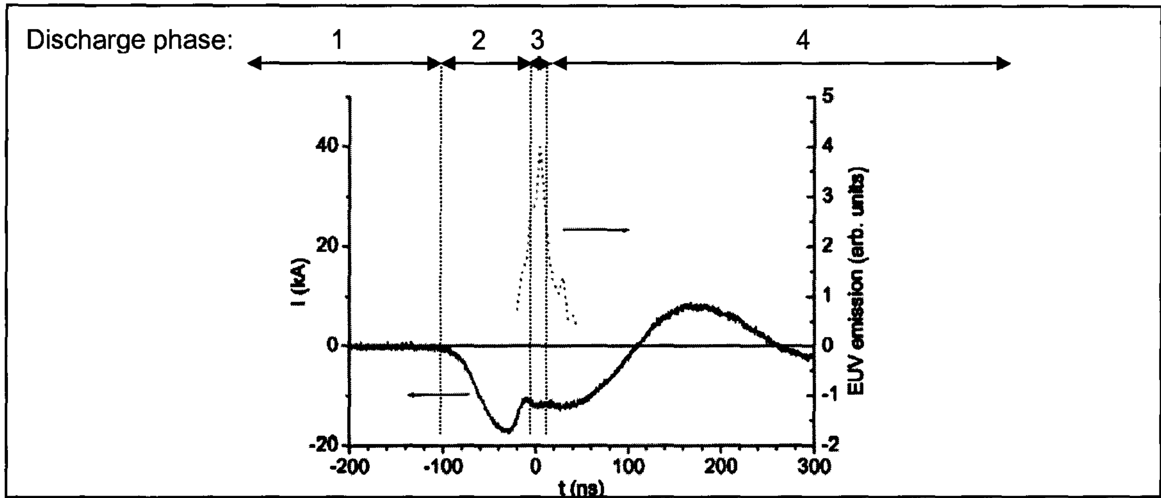

Figure 2.4 Discharge current (solid curve) and EUV emission (dashed curve) during the discharge. The current is derived from the electrical circuit parameters and is only approximate. The center of the pinch phase is chosen to be zero on the time scale. On top the discharge phase is shown with 1. the ignition phase, 2. the prepinch phase, 3. the pinch phase and 4. the decay phase [9].

3. Debris

3.1 Introduction

The Sn-source generates not only EUV-light but also produces debris that damages the optics resulting in a decrease of the EUV reflection and thus a reduction of the available EUV power. It is the aim of this study to find means to reduce the debris such that the decrease of the reflection after 10^9 shots is not larger than 10 %.
The anode/cathode erosion together with the discharge plasma are the main contributors to the total amount of debris. An overview of some theories that describe anode and cathode erosion will be given in this section together with some models concerning plasma plume propagation.

In general one can distinguish between three types of debris and their effect on the optics:

1. Micro-particles $\Rightarrow$ Locally non-uniform collector surface coverage
2. Slow atomic-ionic $\Rightarrow$ Uniform collector surface coverage
3. Fast ionic-atomic $\Rightarrow$ Collector surface sputtering and implantation

For each type of debris the effect of the impact on the optics is different but they all result in reflection loss. The micro-particles, also called particulates or droplets, will result in a locally non-uniform surface coverage. The slow atomic-ionic debris will deposit on the mirror and results in a uniform surface coverage while the fast ionic-atomic debris results in sputtering of and implantation into the surface.

The damage caused by the micro-particles and fast ionic-atomic debris is irreversible. The deposition by the slow atomic-ionic debris can be removed using a cleaning strategy. The irreversible damage caused by fast ionic-atomic debris and micro-particles has to be suppressed to 5×10^9 shots. However the reversible damage caused by deposition should be suppressed to a value satisfying the mean time between cleaning. The latter is determined by the requirement for the EUVL system down time and is about 10^8 shots.

Different experiments have been performed to characterize the debris. In section 3.3 the characteristics of the micro-particles are presented. A sample has been exposed to the Sn-source and using Scanning Electron Microscopy (SEM) the micro-particles were visualized. From the results of the experiments with the rotating foil trap (RFT) in section 4.1.2.2 and with software developed at ISAN [16], the speed of the particles with respect to their size was determined.

The amount of the slow atomic-ionic debris produced by the source was measured in section 3.4. With a setup where the RFT was used in combination with a Quartz Crystal Microbalance (QCM), it has been shown that about 50 % of the total mass of the deposited debris is due to the slow atomic-ionic debris. Then the amount of slow atomic-

ionic debris produced by the source was calculated using X-Ray Fluorescence (XRF) on a sample.

In section 3.5 a faraday cup (FC) has been used to characterize the ionic debris. The FC has a set of three grids. When a positive voltage is applied to the second grid, it should be possible to analyze the energy of the ions. However no conclusions could be drawn from these experiments. With the use of time of flight (TOF) measurements and with the FC placed at several different distances from the source, the minimum and maximum energies of the ionic debris was measured.

3.2 Origin of the debris

The slow and fast atomic-ionic debris originates from the discharge plasma. Because of the compression of the plasma during the pinch phase, a lot of the pinch material is pushed away in the axial direction. This ion bombardment leads to a vaporization of the anode material and micro-particle ejection at the liquid cathode surface.

Numerous articles about anode or cathode erosion and plasma plume propagation have been published. Most of the models that describe the behavior of atomic debris are based on laser ablation or a laser-induced plasma. In our case the laser is only used to evaporate the liquid Sn and the plasma is generated by a discharge through the Sn plume. When using the source not only a decrease in the level of the Sn-bath was observed but also significant erosion of the anode (figure 3.1).

In section 3.2.1 some models are presented that describe the anode/cathode erosion and the resulting droplet formation. Section 3.2.2 gives an overview of some articles that describe plasma plume propagation and droplet formation in the expanding plume.

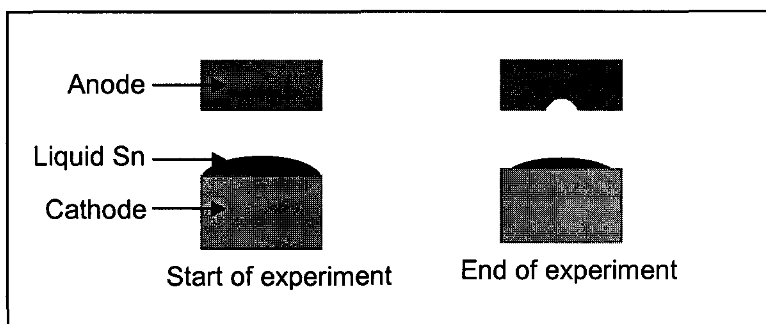

Figure 3.1 After experiments a decrease in the level of the Sn on the cathode and an erosion of the anode was observed.

3.2.1 Anode/Cathode erosion

The erosion of the Mo-anode is ascribed to a heat flux from the plasma to the anode surface and vaporization of the anode material [11]. Then an ion bombardment of the anode and cathode after the pinch, can result in a micro-droplet ejection [12]. The heat flux can be described using two different models:

1. A two-dimensional thermal model for cylindrical Mo-anodes has been published [17]. The model includes heat flux from the plasma to anode surface, radiation from surfaces of the whole anode and temperature-dependent thermo physical coefficients of the anode material.

2. A point heat source model differs from conduction models in that it accepts power rather than temperature as the boundary condition at the plasma-anode/cathode interface [18] [19]. A constant fraction of the total power supplied to the gap is assumed to be transferred to the anode/cathode. The power produces a Gaussian-distributed heat-flux on the surface of the anode/cathode material.

Droplet formation is extensively studied in the case of gas metal arc welding (GMAW), which uses a discharge between a metal electrode and the weld pool. Two major models are developed to describe the droplet formation and detachment in the case of GMAW: the static-force balance theory (SFBT) and the magnetic pinch instability theory (PIT). The SFBT considers the balance between gravity, electromagnetic forces, plasma drag force and surface tension acting on a pendant drop. The PIT considers perturbation due to the magnetic pinch force acting on an infinite cylindrical column of liquid metal [20].

3.2.2 Plasma plume

Different articles present a discussion about various models concerning the laser evaporated plume expansion in vacuum [21] or in a background gas [22]. The general effect of a background gas is reported to be the spatial confinement and slowing down of the expanding plume. The plasma plume may be split into two components; a fast component that consists of ions and atoms that have not collided with the background gas, and a slow component of which the velocity is reduced due to the interaction of the plume with the background gas [23] [24].
The major part of particulate formation is expected to be at the cathode surface but a number of models describe particulate formation and growth in the expanding vapor plume [22]. Particulate formation is expected when the background gas pressure is sufficiently high, so that many collisions can occur, although condensation can take place under vacuum conditions as well [25].

3.3 Micro-particles

3.3.1 Introduction

The micro-particles or droplets generated by the source are the first type of debris that will be discussed. This kind of debris is often referred to as droplets or particulate debris, because each particle consists of a number of Sn atoms. The micro-particles originate from the cathode surface, because of the ion bombardment after the pinch. The moving direction of the particulate debris overlaps with the EUV photons. The particles stick to the EUV optics and this results in a locally non-uniform collector surface coverage.

Because the collector mirror will be placed in a grazing angle, the non-uniform coverage will result in a larger effective coverage. When the light hits the collector under an angle of about 10 degrees (figure 3.1) the shadow of the droplet increases the effective coverage ratio with a factor of 5. That is to say, the EUV photons will experience a coverage that is a factor of 5 higher than the actual one.

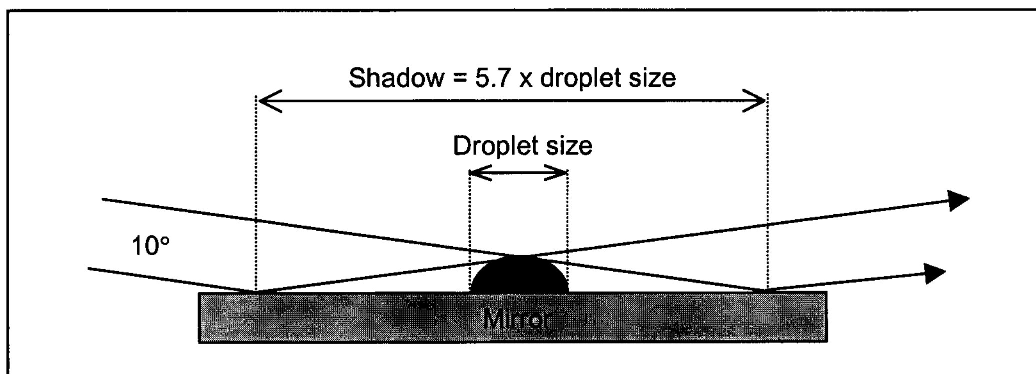

Figure 3.1 The effect of droplets on the reflectivity of a mirror when it is placed in a grazing angle of 10 degrees.

In order to visualize the droplets, a sample has been exposed to the Sn-source and with a Scanning Electron Microscopy (SEM) images were made. With the use of software developed at ISAN is was possible to determine a coverage ratio and to count the droplets according to their size [16].

A velocity spectrum of droplets emitted by a liquid-metal cathode has been investigated by Popov using a setup that separates the droplets by their velocities [26]. The velocities that were measured are in the range of 10-800 m/s and it has been found that small droplets in general have higher speeds than the larger ones. A relationship between the maximum velocities and the drop diameter D for droplets emitted by a mercury cathode

is approximated by the following equation were v_{max} is measured in m/s and D in μm and $c = 50$

$$v_{\max} \approx \frac{c}{\sqrt{D}} \tag{3.1}$$

3.3.2 Experiments

Figure 3.2 shows a SEM picture of a Si-sample directly exposed to debris of the Sn-source. The picture clearly shows the micro-droplets with sizes up to 10 μm. From such pictures it is possible to count the particles according to their size and to determine a coverage ratio.

The sample was placed at a distance of 160 mm from the pinch and directly exposed to the debris for about 250 kshot under vacuum conditions (10^{-5} mbar). Figure 3.4 shows the setup for this experiment. The coverage ratio from the droplets on figure 3.2 was 2.30 %. When the correction is applied for a 10 degrees grazing angle the effective coverage is about 11.5 % at a distance of 160 mm from the source. In order to fulfill the lifetime demands, the maximum allowed effective coverage is 10 % after 5×10^9 shots. This clearly indicates the importance of the droplet mitigation for the lifetime improvement of the EUV-optics.

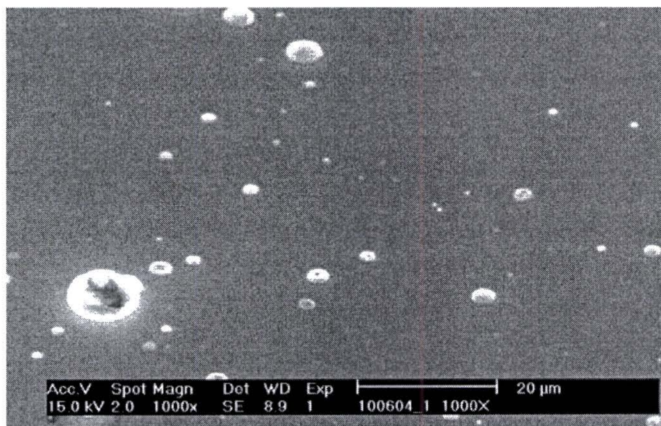

Figure 3.2 A SEM picture of sample nr.1 exposed to the debris as shown in figure3.4. The picture has a magnification of a factor 1000. The Sn-droplets, with sizes up to 10μm, can be clearly seen on the surface.

In order to get information about the *speed* of the droplets we used a device, the rotating foil trap (RFT), that will also be applied for mitigation purposes. The six samples from the RFT experiment with 10 sccm Ar in section 4.1.2.2 were analyzed using software

developed at ISAN [16]. The software made it possible to count the particles according to their size. During the exposure of each sample a higher rotation speed of the RFT was used. When a certain droplet size wasn't present on a sample, the maximum speed of droplets with that size was considered to be equal to the stopping speed of the RFT (information about the working principle of the RFT can be found in section 4.1.1). Figure 3.3 shows the maximum speed of the droplets versus their size. It has been found that small droplets have higher speeds (up to about 650 m/s) than the larger ones. The line shows a fit of equation 3.1 with v expressed in m/s, D in μm and with $c = 250$. For particles with size $D < 3$ μm the fit is in reasonable agreement with the experimental results.

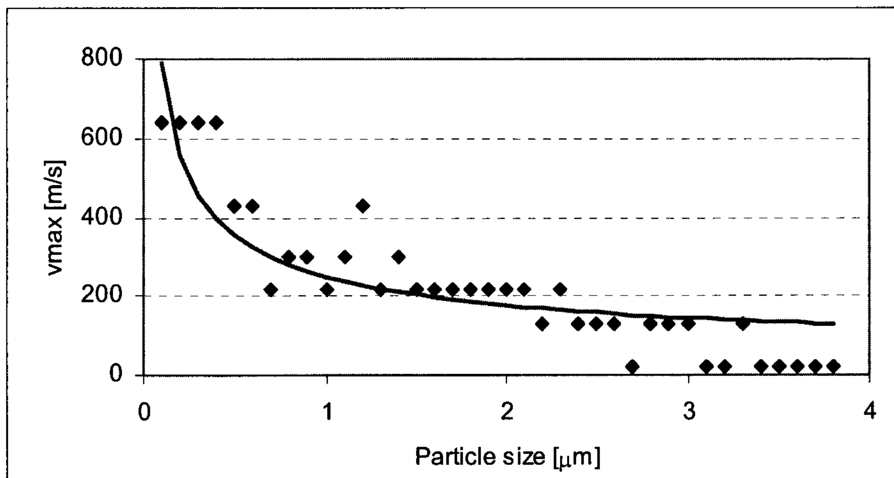

Figure 3.3 The maximum speed of the droplets according to their size. The line is a fit of eq. 3.1 with $c = 250$ and is a reasonable approximation for particles < 3 μm.

3.4 Slow atomic-ionic debris

3.4.1 Introduction

Slow atomic-ionic debris consists of neutral atoms as well as low energy ions. In contrast to the particulates that are created at the electrode surfaces, these particles are generated by the plasma and are thermalized. This means that they have randomized directions and velocities according to the Maxwell velocity distribution. The deposition on the collector of this kind of debris, results in a uniform surface coverage. The loss in reflectivity of the collector mirror is relative to the thickness of the deposited layer. For example 1 nm of Sn on a Ru-mirror results in a reflection loss of 14% for a grazing angle of incidence of 10 degrees [27]. Thus in order to reach a mirror lifetime of 10^8 shots, no more than 1nm of Sn may be deposited on its surface.

A rotating foil trap (RFT) has been used in combination with a Quartz Crystal Microbalance (QCM) to determine the total amount of mass of the deposited atomic-ionic debris. Then the amount of slow atomic-ionic debris produced by the source was calculated using X-Ray Fluorescence (XRF) on a sample. A schematic of the setup is shown in figure 3.4.

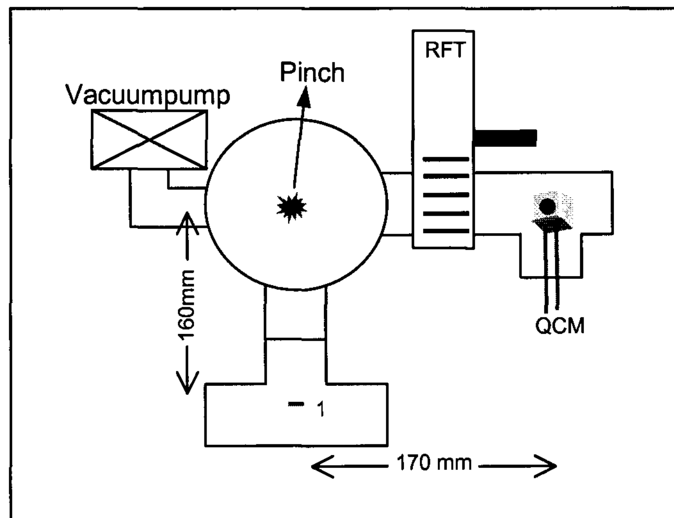

Figure 3.4 Top view of the setup used to characterize the debris, in particular the micro-droplets and slow atomic debris. On the left the vacuum pump is connected to the vacuum chamber. On the bottom a Si-sample (nr.1) was directly exposed to the Sn source. On the right the rotating foil trap (RFT) was used to mitigate the droplets. With a Quartz Crystal Microbalance (QCM) the amount of atomic debris could be measured.

3.4.2 Experiments

The QCM was operated with a control unit (MAXTEK TM-350) which makes the crystal vibrate at its resonance frequency. Whenever material is deposited on the crystal, its mass changes and so does its resonance frequency. The control unit detects the change in resonance frequency of the crystal and recalculates this to a thickness of the material deposited on the crystal (see appendix A).

The RFT was used to stop the major part of the micro-droplets (up to a speed of 350 m/s) so it could be estimated from the QCM measurements which part of the debris is atomic. Each measuring series has a different color and each individual point has 9000 shots or more. The series all started with a reference measurement with no rotation of the RFT followed by measurements with rising rotating speeds of the RFT. Figure 3.5 shows the suppression of part of the debris by the RFT. The line shows the trend in the measurements. It can be seen that about 50% of the total mass of the deposited debris is due to droplets, leaving another 50% atomic debris.

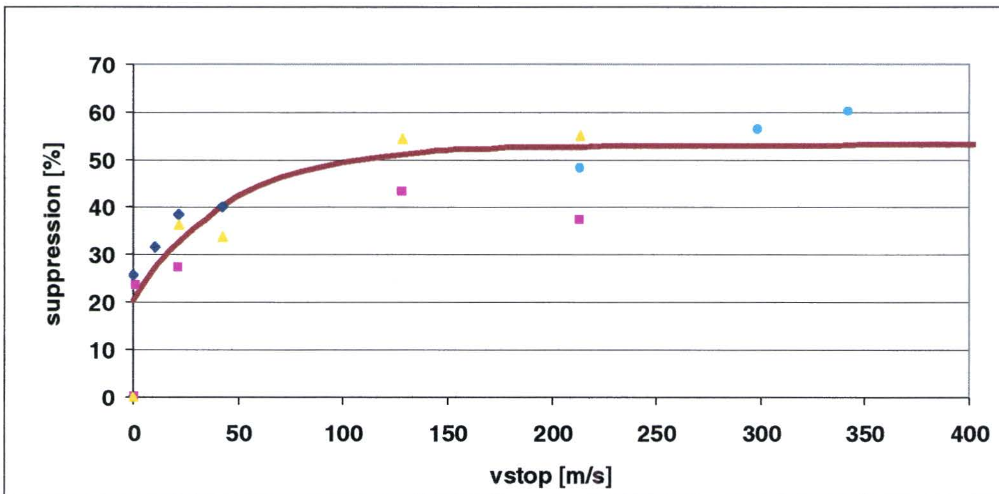

Figure 3.5 Suppression of debris by the RFT, measured with the QCM. The line shows the trend in the data. About 50% of the total mass of the debris is due to droplets, leaving another 50% of atomic debris deposited on the QCM.

The sample from figure 3.2 that was exposed to the source as seen in figure 3.4, was analyzed using X-Ray Fluorescence (XRF). The total amount of debris under the X-ray beam, in this case with a diameter of 10mm, was determined to be 100 $\mu g/cm^2$ Mo and 36 $\mu g/cm^2$ Sn. The large amount of Mo present on this sample, is due to the position of the sample in a perpendicular direction to the half round Mo-anode. In the newly developed Sn-based EUV-sources both electrodes will be made of Sn [28]. The total amount of slow atomic-ionic debris produced by the source is thus equivalent to about 5×10^{15} atoms/shot in a solid angle of 4π directly at the source.

3.5 Fast ionic-atomic

3.5.1 Introduction

Fast ions and in a less amount neutrals generated by the plasma cause a reduction in reflectivity of the mirror material. This kind of debris results in sputtering of and implantation into the surface. Again the maximum allowed reflection loss is 10% after $5x10^9$ shots.

Two different approaches were used to measure ionic debris. The first is an ion energy analyzer based on a cylindrical capacitor designed at ISAN and the second is a Faraday Cup (FC). These kind of detectors together with the Time of flight (TOF) analysis are commonly used in many fields [29] [30] [31]. The experiments with the ion energy analyzer have been performed by researchers at ISAN and a summary of the results is presented next.

The ions from the ISAN Sn-source were characterized using an ionic energy analyzer to deflect the ions according to their charge state. It has been found that ions with charge Z=1 to Z=10 were present in the ionic debris and they have energies up to several keV. The ionic spectrum was found to be weakly dependent on the trigger laser energy density, which was focused on the cathode surface.

3.5.2 Faraday cup experiment

The ion measurements have been performed with the use of a faraday cup with length 5 mm and diameter 5 mm (Kimball Physics model FC-73A). The cup was placed at various distances from the source and connected to an oscilloscope to measure the charged particle current, emitted by the Sn-source. The FC has a set of three grids so that it can be used as an energy analyzer (figure 3.6). The first grid is grounded to increase the stability of the electrical field from the second grid, the retarding grid. A variable potential up to 5 kV can be applied to the retarding grid to analyze the energy of the ions. The FC current at any given retarding grid potential represents the total current due to the ions with energy greater than that potential. When a voltage is supplied to the third grid, the suppression grid, it can be used to suppress secondary and scattered electrons so that current is not lost. Instead of applying a voltage to the suppression grid, the FC can be electrically biased to reduce scattering of ions collected in the FC and to reduce secondary electron emission.

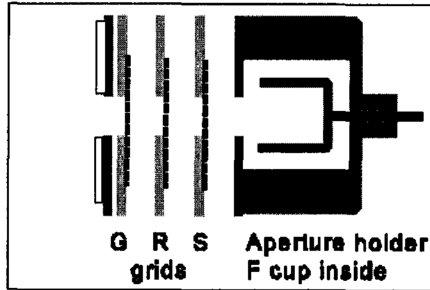

Figure 3.6 Schematic of the FC-73A. The grounded (G), retarding (R) and suppression (S) grid are positioned in front of the grounded aperture holder (∅ = 5.0 mm).

Experiment

The ionic debris was characterized using the FC-73A placed at a distance of 50 cm and 30 cm from the pinch. The FC was connected to an oscilloscope and for each scan the average of 8 shots from the source was used. The experiments were performed under vacuum conditions (10^{-5} mbar). The cup was electrically isolated from the setup to reduce noise coupling into the signal. A voltage V_R was applied to the retarding grid and the FC was biased with a voltage V_C. Figure 3.7 shows the FC signal for V_R = 0 V and V_C = 0 V.

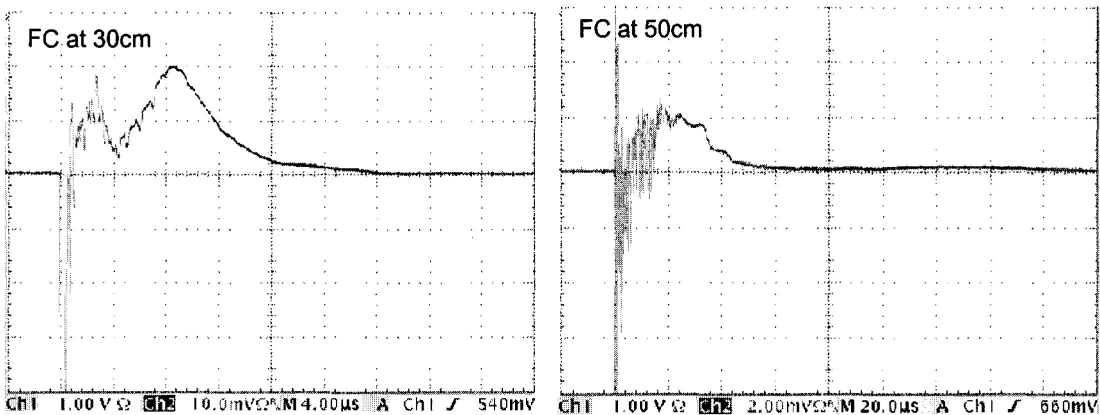

Figure 3.7 Signal of the FC-73A placed at 30 cm and 50 cm from the pinch and for V_R = 0 V and V_C = 0 V. Mind the different vertical scales for CH2 when comparing the pictures. A time scale of 4 μs and a vertical scale of 10 mV is used on the left and a time scale of 20 μs and a vertical scale of 2 mV on the right picture.

When applying a voltage to the retarding grid, the FC signal quickly drops and reaches zero around 0.3 kV. It is clear that this voltage is not high enough to actually stop the incoming ions. Therefore, an alternative explanation for the dropping signal has to be assumed: electrons can be drawn to the cup by the positive retarding grid voltage. This made it impossible to characterize the ions in their energy with the retarding grid.

Applying a negative voltage to the cup slightly increases the signal intensity and reduces the noise at the beginning of the FC signal. However the length of the signal increases when a negative voltage is applied to the cup, as seen in figure 3.8.

Because of the small signal intensity and the amount of noise into the FC signal, a larger faraday cup (FC-HM) was constructed without any grids in front of the cup. The FC was made of thin copper plate and has the following dimensions: length L = 60 mm and diameter d = 18 mm. A pinhole with diameter d = 9 mm was placed in front of the FC-HM. The cup was placed at a distance of 73 cm from the pinch. The experiments were performed under vacuum conditions (10^{-5} mbar). A voltage V_C was applied to the cup to reduce scattering of ions collected in the FC. Figure 3.8 shows the FC signal for $V_C = 0$ V and $V_C = -1$ V. It can be clearly seen that applying a negative voltage to the cup increases the signal intensity and duration.
With the use of the TOF technique, the energy of the ions collected by the cups was calculated. Table 3.1 shows the results. It has been found that the ions have energies from about 80 eV up to 4.5 keV.

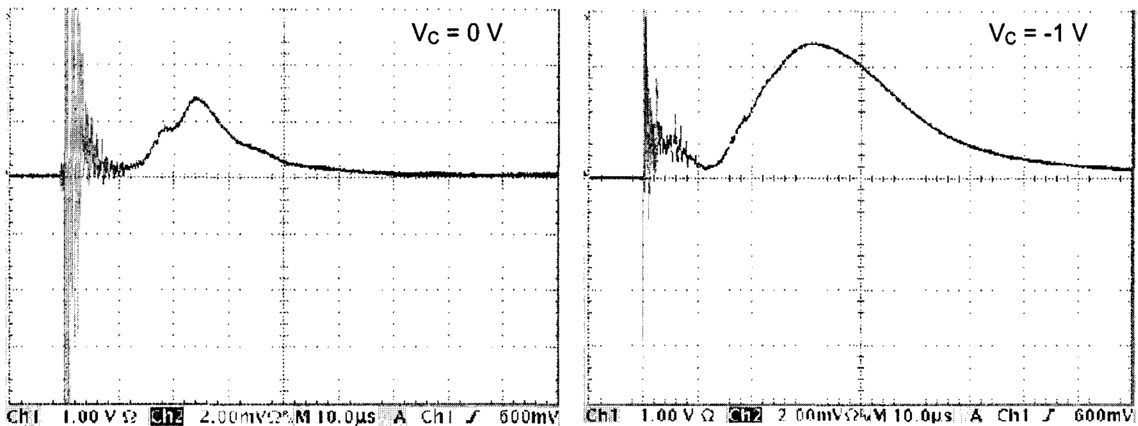

Figure 3.8 Signal of the FC-HM placed at 73 cm from the pinch for $V_C = 0$ V and $V_C = -1$ V. Both pictures have a time scale of 10 µs and a vertical scale of 2 mV.

Table 3.1 Calculation of the ion energy from the FC signal using the TOF technique.

Distance [cm]	Experiment	Vc [V]	VR [kV]		start	end
30	050127_0	0	0	t [µs]	5	24
	FC-73A			v [m/s]	6.0E+04	1.3E+04
				Ekin [eV]	4.5E+03	1.9E+02
50	050128_0	0	0	t [µs]	???	60
	FC-73A			v [m/s]		8.3E+03
				Ekin [eV]		8.6E+01
73	050128_10	0		t [µs]	14	60
	FC-HM			v [m/s]	5.2E+04	1.2E+04
				Ekin [eV]	3.4E+03	1.8E+02
73	050128_15	-1		t [µs]	14	90
	FC-HM			v [m/s]	5.2E+04	8.1E+03
				Ekin [eV]	3.4E+03	8.2E+01

4. Mitigation

It has been shown that the Sn-source produces a lot of debris, which results in a reduction of the EUV reflectivity of the mirrors. This chapter will focus on mitigation strategies for the different kinds of debris. The working principle of each mitigation method is explained first, followed by an explanation and interpretation of the performed experiments. The different mitigation schemes include:

1. A rotating foil trap (RFT)
2. A reflective foil trap
3. A gas controlled stationary foil trap (SFT)

Because of the large amount of particulate debris, the mitigation of particulates becomes as important as the mitigation of the atomic-ionic debris. A new mitigation method, the *RFT*, was developed especially dedicated to stopping particles with a ballistic nature like micro-droplets. It is used in combination with a *SFT* to stop the micro-particles with a vertical velocity component. The SFT can be filled with a *background gas* (Ar) so that a device is constructed that is capable to mitigate the atomic-ionic debris

The idea of the *reflective foil trap* is that it stops the micro-particles and that the EUV photons are transmitted through reflection by the foils. The foils are aligned in such a way that the reflection of EUV photons is as large as possible and that all the micro-particles will hit the foil under an angle at which the particles stick to the foil. Unlike the RFT, the reflective foil trap will mitigate the micro-particles without the need to rotate the foils. If a gas is injected in the reflective foil trap it will have the same working principle as a gas controlled SFT for mitigation of the atomic-ionic debris.

In order to stop the atomic-ionic debris a *SFT* will be inserted with an *Ar buffer gas*. Whenever the atom or ion hits the surface of one of the foils, it sticks there and thus is trapped inside the foil trap. Increasing the pressure of the buffer gas will increase the probability that an atom hits one of the walls. The buffer gas has to be as transparent as possible for EUV photons leaving the plasma. The suppression of atomic-ionic debris by a gas controlled SFT was calculated using two different models.

4.1 Rotating foil trap

The first mitigation setup that will be discussed is the *rotating foil trap* (RFT). The RFT will only be effective against particulate debris and has to be used in combination with a *stationary foil trap* to stop the micro-particles with a vertical velocity component. The effect of the mitigation was determined by means of measuring the coverage ratio on a sample. For this we performed two series of experiments. The first series was performed at ASML and to determine more effectively the coverage ratio, some experiments were performed at Philips Extreme UV [32] in a set-up with a Sn-source having a higher repetition rate.

4.1.1 RFT principle

The working principle of the RFT is rather simple (figure 4.1.1). A rotating foil trap with radius R consists of n thin foils with length L attached to a rotating axis, which is driven by an electric motor. The spacing between the foils increases with the radius r of the foil trap with b the maximum spacing at the foil tip. The linear velocity of one foil tip v_{lin} is then given by

$$v_{lin} = f_{RFT} \cdot b \cdot n \qquad (4.1.1)$$

where f_{RFT} is the rotating frequency of the RFT. A particle with velocity v_p which is lower than the *(linear velocity of the foil trap)* × *(aspect ratio of the foil trap)* and going in the direction parallel to the foils, will be stopped by the foil trap (fig 4.1.1a). Faster particles will go trough. The highest velocity of a particle that is just being stopped by the RFT is then given by

$$v_p = \frac{v_{lin} \cdot L}{b} \qquad (4.1.2)$$

This velocity will be called v_{stop}. Together with equation 4.1.1 the following expression is found for the maximum velocity of the particles stopped by the RFT

$$v_{stop} = f_{RFT} \cdot L \cdot n \qquad (4.1.3)$$

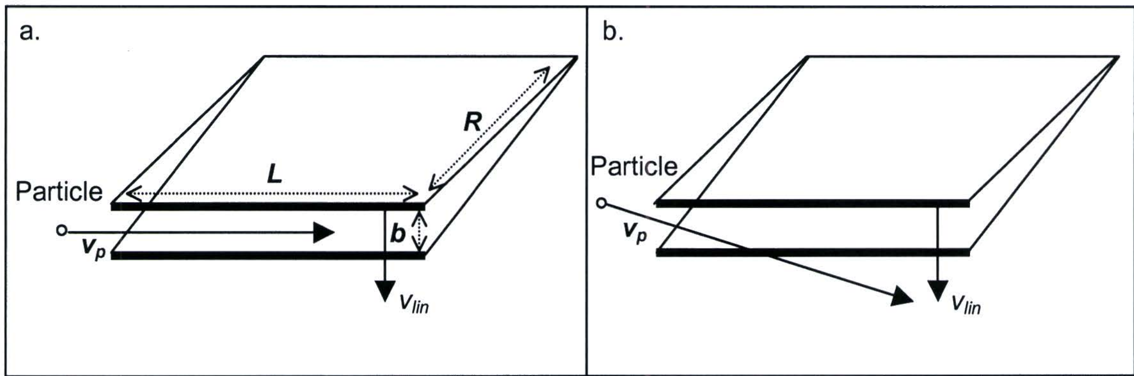

Figure 4.1.1a) Working principle of the rotating foil trap with radius R, length L and spacing b. When the velocity of a particle is lower than the linear velocity of the foil trap it will be stopped. b) A particle with a vertical velocity component matching v_{lin} will go through and has to be filtered away with a stationary foil trap.

Unfortunately there are some particles for which the vertical velocity component matches the linear velocity of the foil trap (fig 4.1.1b). These particles will go through. With a construction of both a *stationary* and a *rotating foil trap* this problem can be solved. The stationary foil trap (SFT) will only be transparent for the particles with a velocity parallel to the foils.
The SFT can be filled with a background gas (Ar) so that a device is constructed that is capable to mitigate the atomic-ionic debris. For the following experiments it only serves for stopping the particles with a vertical velocity component that allows passage through the RFT. Figure 4.1.2 shows the RFT attached to the vacuum chamber. The foils can clearly be seen on the enlarged picture.

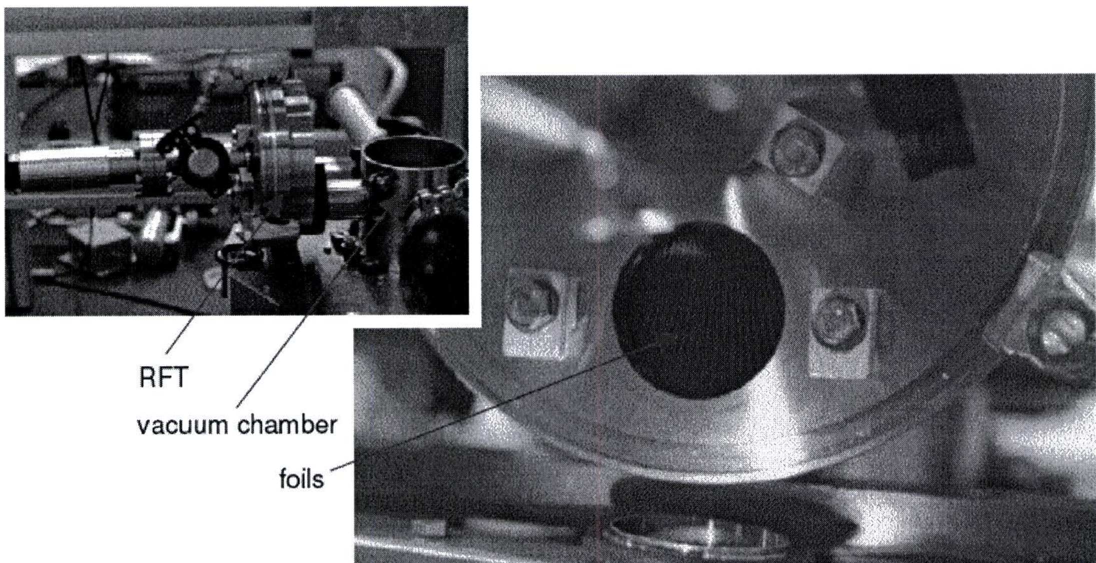

Figure 4.1.2 The rotating foil trap as it is attached to the vacuum chamber. The enlarged picture of the RFT shows the foils.

4.1.2 RFT experiments

The RFT used in the experiments has 178 foils, each with a length $L = 48$mm, attached to a central axis driven by a small electric motor. With formula 4.1.3 the relationship between the rotation frequency of the foil trap f_{RFT} and the stopping velocity of the particles v_{stop} can be calculated. This leads to a simple graph in figure 4.1.3. If f_{RFT} is given while explaining some experiments, this figure can be used to see the matching stopping velocity of the particles.

Two series of experiments have been performed. The first series was performed at ASML. The second series are performed at Philips Extreme UV [32] in a set-up with a Sn-source having a higher repetition rate.

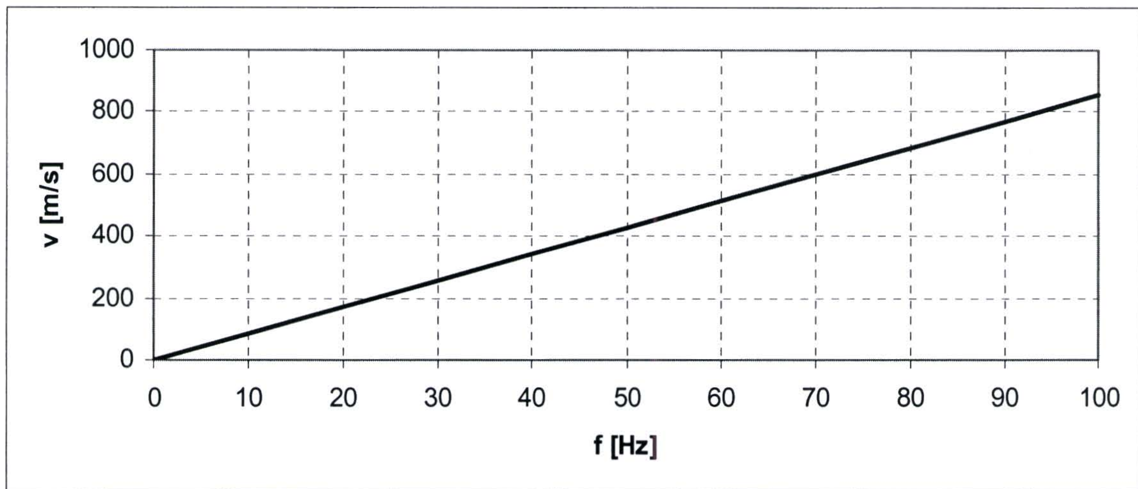

Figure 4.1.3 The rotation frequency of the foil trap f and the maximum velocity of the particles stopped by the RFT.

4.1.2.1 Experiment with the ASML Sn-source

In the first experiment two samples were exposed to the normal incident debris and EUV-light. In this experiment a smaller version of the RFT was used. The maximum stopping velocity of this device was 200 m/s, which corresponds to a rotation frequency of about 25 Hz for the newly designed RFT. The pressure in the vacuum chamber was 2×10^{-5} mbar and 250 kshot were counted while the laser was pulsing at 10 Hz. As said the foil trap was rotating at 25 Hz, which means that all the particles with a speed lower than 200 m/s are stopped.

The samples were analyzed using SEM images. The setup and the SEM images of the experiment can be seen in figure 4.1.3. It can clearly be seen that there is a large difference between the morphology of samples with (low coverage of particles) and without mitigation (higher coverage of particles). All the larger particles seem to be mitigated while smaller ones are still present.

Software developed at ISAN [16] made it possible to count the particles according to their size (fig 4.1.4) and to determine the coverage ratio from these SEM images. Sample nr.1 has a coverage of 2.30% and sample nr.2 has a coverage of 0.35%. The larger particles are stopped while the smaller particles are still present on the sample. This means that the sub-micron particles have velocities larger than 200 m/s. To stop these particles a higher rotation frequency of the foil trap is needed.

Note that with using the 1000× magnification a smaller part of the sample is investigated compared to 50× magnification. This way we look in between the large particles but get a better view on the smaller ones.

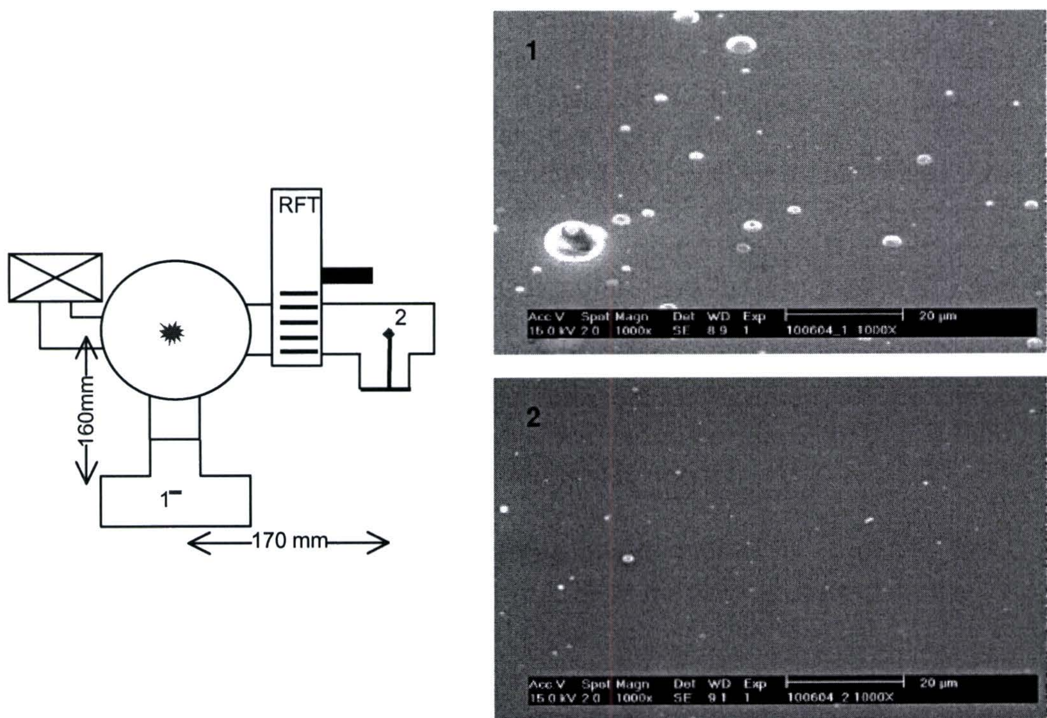

Figure 4.1.3 Setup of the experiments performed with the use of the RFT at 25 Hz. Sample nr.1 is used as a reference sample (the highest SEM image) and sample nr.2 (below) is placed behind the RFT. It can be clearly seen that with mitigation the larger particles are stopped.
Coverage sample nr1: 2.30 %
Coverage sample nr2: 0.35 %

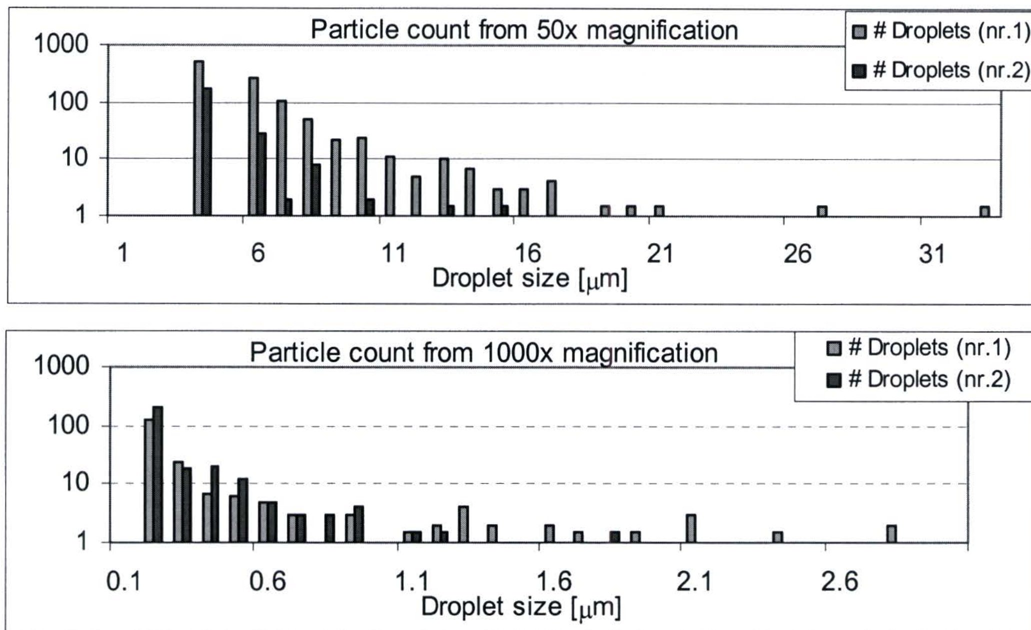

Figure 4.1.4 From the SEM images of 50× and 1000× magnification the particles were counted according to their size. For particles < 1μm there is no mitigation, which means that their velocity is higher than 200 m/s. Note that the values along the vertical axis do not refer to a number of particles per unit of area but the number of particles present on the relevant SEM image.

While raising the rotation frequency of the RFT, the vibrations caused by the rotation grew larger and eventually they disturbed the discharge and from a frequency of 80 Hz the discharge became very unstable. Increasing the frequency of the RFT means that more droplets are mitigated so more shots are needed the see the effect on a sample. One measurement of 250 kshot with the ASML Sn-source at its highest pulse rate of 10 Hz, takes about 7 hours. During the experiment the laser position has to be changed because of erosion of the anode and after the experiment the level of the Sn bath had decreased a few millimeters. This means that the distance between the anode and cathode increases significantly, causing a decrease in the EUV-signal monitored with the photodiode and results finally in an unstable discharge. To avoid all these problems the RFT was tested in collaboration with Philips Extreme UV [32] in a set-up with a Sn-source having a higher repetition rate (up to 400 Hz) and a larger vacuum chamber so the vibrations wouldn't have any effect on the discharge.

Before performing the experiment with another source, two reference samples, one exposed to the ASML-source and one to the Philips-source, were compared to ensure that the amount of particulate debris from the two different sources would be similar. Figure 4.1.5 shows the particle count that has been performed for both samples. The number of particles is normalized to the number of particles that would have been on the sample after 1 Mshot at a distance of 16 cm from the source.
It was found that the micrometer-sized particles are about the same but the number of sub-micron particles on the sample exposed to the Philips source is a factor of 10 higher.

This indicates towards a problem with the source, however for the experiment this was very convenient.

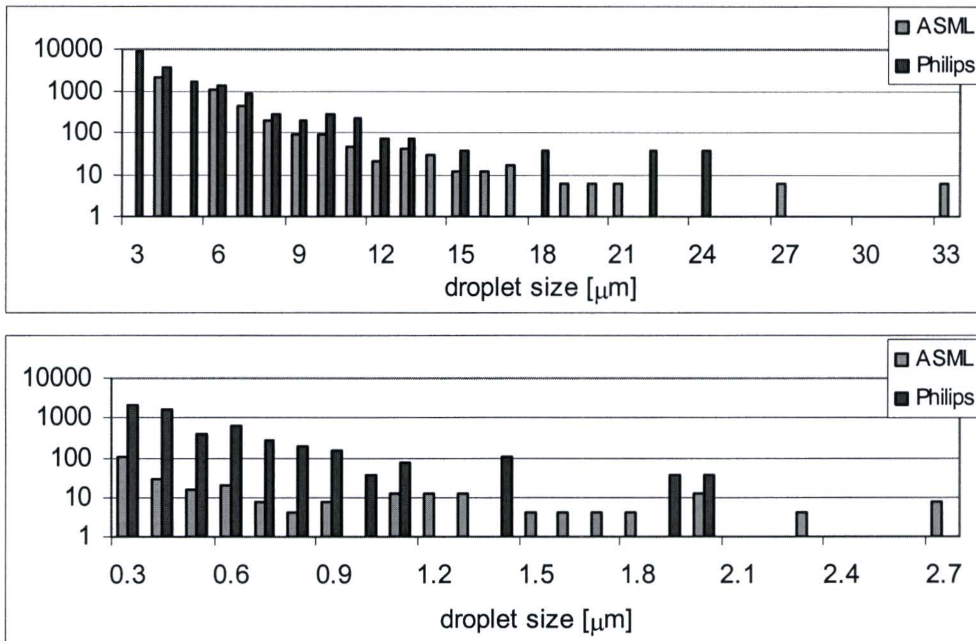

Figure 4.1.5 Particle count from samples exposed to the ASML and Philips source without mitigation, normalized to the same conditions. There are more small (< 1μm) particles on the samples exposed to the Philips source.

4.1.2.2 Experiment with the Philips Sn-source

The particle mitigation experiments were repeated for various speeds of the rotating foil trap (RFT). Figure 4.1.6 shows the setup. Two series of experiments have been performed. One under vacuum conditions (pressure < 10^{-5} mbar) and one with an Ar flow of 10 sccm, which corresponds to an average pressure of 2×10^{-2} mbar inside the stationary foil trap (SFT). The samples were analyzed using SEM images and X-Ray Fluorescence (XRF). With XRF the total amount of debris under a X-ray beam is determined and the results can be used to see if there were irregularities during the experiment.

If the RFT should prove to be successful at suppressing the micro-particles, then the XRF measurement of the samples can give a suppression rate of the slow atomic-ionic debris by the SFT injected with 2×10^{-2} mbar Ar gas.

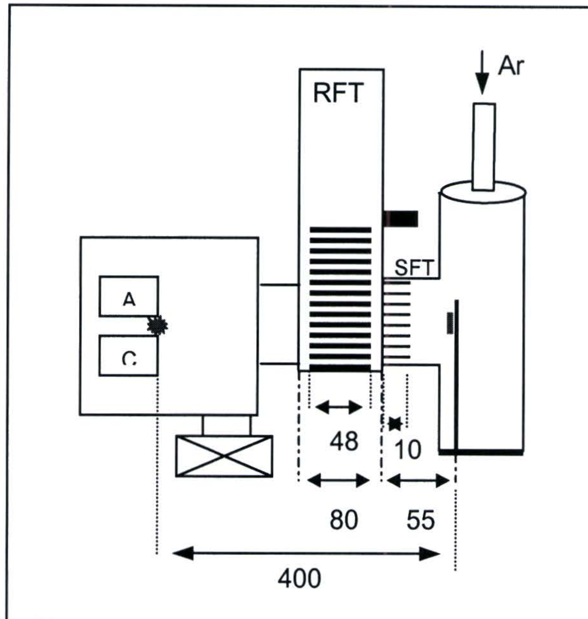

Figure 4.1.6 Topview of the setup used to perform the experiments with the Philips Extreme UV Sn-source. The sample is at a distance of 400 mm from the discharge between the anode (A) and cathode (C). A stationary foil trap (SFT) of 10 mm length is placed behind the RFT. The Ar-inlet is shown at the top of the picture.

Figure 4.1.7 shows four SEM images with 2000× magnification of some samples placed behind the RFT. The images show that the RFT in combination with the SFT is capable of suppressing the particulate debris for all relevant droplet sizes. The coverage of the exposed sample with rotation frequency 75 Hz is well below the background dust level. The SEM image that was taken of this sample shows some droplets.
While looking for these droplets, more *dust* particles than tin droplets were found. The software that is used to analyze the images doesn't make any difference between dust particles and droplets. If the number of droplets on the sample is very low, the number of dust particles (coverage of about 0.01%) will determine a limit for the measurement accuracy for the used samples.

Table 4.1.1 gives an overview of the experiments and the corresponding results for each sample. Because various exposure times have been used the results for the coverage and XRF are normalized to match 1 Mshot. When comparing the coverage ratio of the samples with the RFT frequency at 2 Hz it seems that with the Ar gas present in the vacuum chamber more droplets are produced. However at a rotation frequency of 75 Hz the coverage ratio of the droplets is below the background dust level. The extra droplets produced by the presence of the Ar gas do not form any problem for the mitigation.

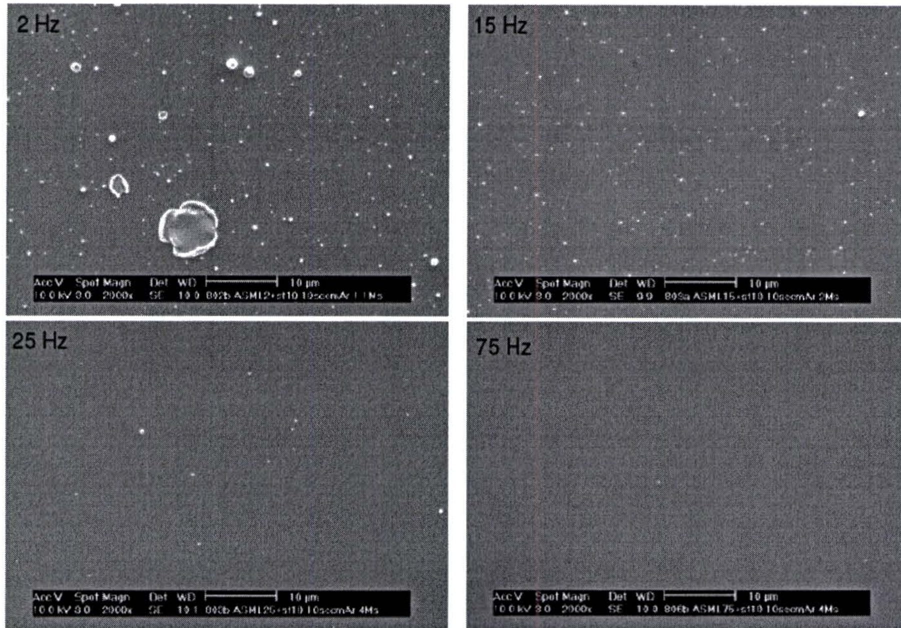

Figure 4.1.7 SEM images of a sample after the RFT at a frequency of 2, 15, 25 and 75 Hz. The magnification is 2000×. The images show that the RFT is capable of suppressing the particulate debris for all relevant droplet sizes.

Table 4.1.1 Overview of the experiments performed with the Philips source. Because of the different exposure times, the coverage and the XRF results were normalized to match 1 Mshot. At 75Hz more dust particles than tin droplets were found and thus the coverage is well below the background dust level, which has a coverage of 0.01 %.

Vacuum			**Coverage**	**XRF (Sn)**
RFT [Hz]	Sample	Mshot	% / Mshot	nm/Mshot
2	Ru040728a	0.5	1.23	26.2
15	Ru040802a	2.0	0.20	8.9
25	Ru040730b	3.0	0.03	2.9
50	Ru040729b	3.0	0.01	6.1
75	Ru040730a	1.1	0.18	14.0

10 sccm Ar			**Coverage**	**XRF (Sn)**
RFT [Hz]	Sample	Mshot	% / Mshot	nm/Mshot
2	Ru040802b	1.1	5.54	6.6
15	Ru040803a	2.0	1.88	1.1
25	Ru040803b	4.0	0.08	0.7
35	Ru040804a	4.0	0.04	0.7
50	Ru040805a	4.0	0.02	0.7
75	Ru040806b	4.0	0.01	0.9

The results of the vacuum measurement show irregularities. This may be caused by sample misalignment or sticking of the foils due to rotation. The results of the experiments with the Ar flow are more consistent. Therefore these will be used to analyze the coverage ratio. From the XRF results can be clearly seen that with an Ar flow there is less atomic debris deposited on the sample. To calculate a suppression rate for the atomic debris, the XRF results for the measurement with and without Ar flow should be compared. Because of the irregularities in the vacuum results this would give a suppression rate with large uncertainty. A suppression rate of atomic debris by a stationary foil trap injected with Ar-gas is further discussed in section 4.3.

A coverage vs. stopping velocity graph is shown in figure 4.1.8. The data point at 640 m/s is below the accuracy limit of the measurement shown by the gray line. The red line indicates the trend in the data and it clearly shows that when all the particles with a speed up to 640 m/s are stopped the coverage ratio comes near to the desired value of 0.002% coverage with 10^6 shots, indicated by the green line. This value corresponds to the goal of 10% coverage with 5×10^9 shots.

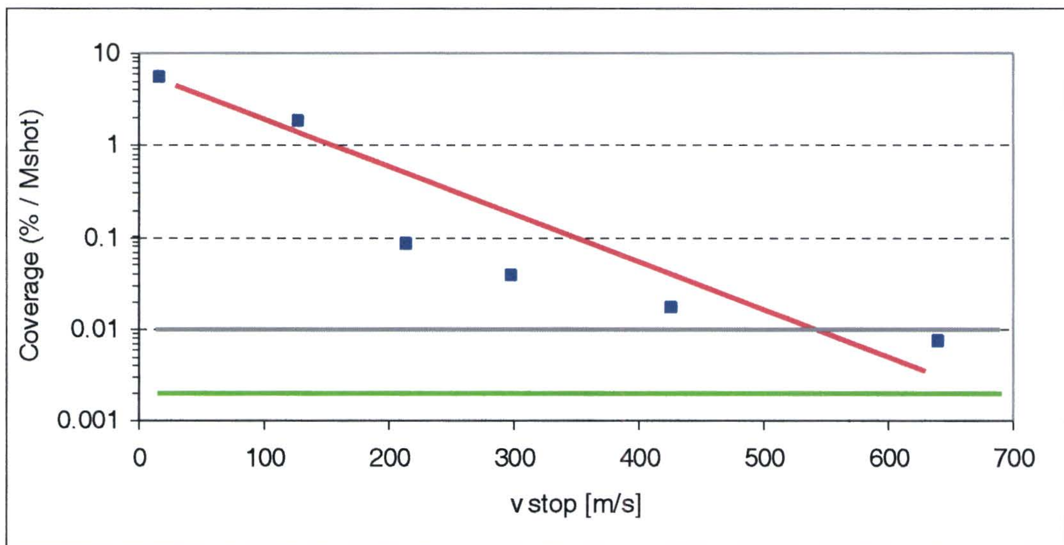

Figure 4.1.8 The coverage ratio in function of the stopping velocity of the particulate debris. The coverage is recalculated to 10^6 shots. The last data point is below the accuracy limit of the measurement, indicated by the gray line. The red line shows the trend in the data and approaches the goal target, indicated by the green line.

4.2 Reflective foil trap

The *reflective foil trap* [33], in which the foils are deliberately misaligned with respect to the source, is constructed to transmit the EUV light through reflection while mitigating particle debris. In order to reduce the atomic/ionic debris a buffer gas has to be inserted to the foil trap. This method is further treated in section 4.3 because it is similar to the case of a stationary foil trap with parallel foils inserted with a buffer gas.

Building a complete reflective foil trap that is also optimized for EUV transmission and minimum pinch deformation is time consuming and it will therefore take a relatively long time until experimental data about debris mitigation can be obtained. Therefore two separate experiments have been performed. In the first experiment a Sn-coated Mo-plate is placed in a small grazing angle in order to measure the reflectivity coefficient. Next a stationary foil trap structure placed close to the source was used to test the particle mitigation of the reflective foil trap. Before performing the latter experiment, the transmission of droplets through the foil trap structure was estimated using a two dimensional point source model and an extended point source model.

4.2.1 EUV reflection experiment

4.2.1.1 Introduction

The amount of light reflected by an object, and how it is reflected, is very dependent upon the smoothness of the surface. When surface imperfections are smaller than the wavelength of the incident light, all of the light is reflected equally. However when the surface roughness is larger than the wavelength of the incident light, the light is reflected in all directions. The reflection of light can be roughly categorized into two types of reflection:

- Specular reflection is defined as light reflected from a smooth surface at a definite angle.
  With this type of reflection a minimum of the available EUV power is lost.
- Diffuse reflection is produced by rough surfaces that tend to reflect light in all directions.
  This type of reflection has to be minimized as much as possible.

To know how well the reflective foil trap will reflect the EUV photons, a thin Mo-plate was used to determine a reflection coefficient of EUV-light under various angles of incidence. However the Mo-plate has a surface roughness of 70-80 nm and thus it will induce a lot of diffuse reflection [34]. To smoothen its surface, the Mo-plate was coated

with a Sn-layer by exposing it to 150 kshot of the Sn-source. Then the plate was heated above 300 °C so the liquefied Sn fills up the surface holes and thus decreases the surface roughness. The reflection experiment has been performed with the coated as well as with the uncoated Mo-plate. Finally the coated Mo-plate was heated during the experiment, so that the surface would consist of liquid Sn and thus canceling out most of the diffuse reflection.

4.2.1.2 Experiment

Figure 4.2.1 shows the setup used to measure the reflectivity. The Mo-plate (10 × 30mm) was placed with a grazing angle α to the incident light. A pinhole with an aperture size of 3 mm was placed between the source and plate. The pinhole was covered using a Nb-filter (Niobium) with a tickness of 150 nm. The Nb-filter has a transmission coefficient of 0.48 at a wavelength of 13.5 nm [Appendix B]. Behind the Mo-plate a UV-sensitive foil (GAFCHROMIC Dosimetry Media, type HD-810) was placed that absorbed the incident light. This way an image can be made of the reflected EUV light. One should realize that the Mo-plate does not cover the complete EUV beam. The intensity of the part that directly goes to the UV-foil is described by I_{aa} in equation 4.2.1. The pressure in the vacuum chamber was 2×10^{-4} mbar and for each measurement 60 to 90 pulses were counted.

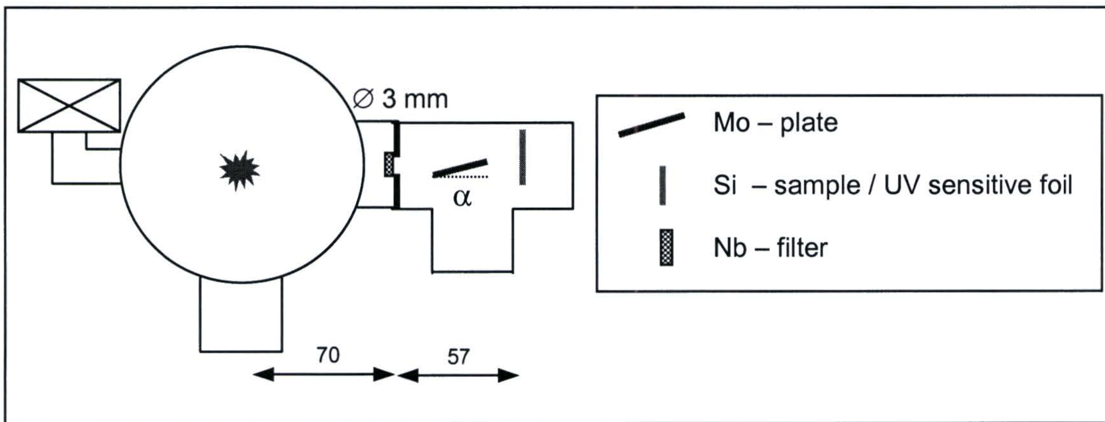

Figure 4.2.1 The setup used to measure the reflectivity of a Mo-plate. A Niobium-filter is placed in front of a pinhole with an aperture size of 3mm. The Mo-plate is placed under an angle α with respect to the dotted line. The reflected light is captured using a UV sensitive foil.

The UV-foils were scanned into a computer and the intensity of the absorbed light was calculated using Mathcad and compared to a reference image of the pinhole. The reflectivity coefficient is then approximated by the following formula

$$R = \frac{I_{cc}}{I_{bb} - I_{aa}} \tag{4.2.1}$$

with I_{aa} the intensity of the non reflected light, I_{bb} the intensity of the reference image and I_{cc} the intensity of the reflected light. The major part of the reflected light intensity is caused by specular reflection. Diffuse reflection scatters the light in all directions so the small contribution to I_{cc} can't be seen on the foil. Figure 4.2.2 shows the image and intensity of the reference image (left) and from a reflection measurement (right).

Due to the difficulty of aligning the Mo-plate in front of the pinhole, the angle of incidence α has an uncertainty of 1°, which results in a maximum error of 0.07 on the measured reflectivity coefficient. Table 4.2.1 gives an overview of the experiments and theoretical calculated reflectivity values for a given roughness of a mirror placed under an angle α [27]. For the un-coated Mo-plate a roughness of 57 nm gave the best fit and for the Sn-coated Mo-plate a roughness of 5 nm gave the best overall result. Table 4.2.2 shows the influence of the roughness on the theoretical reflectivity coefficient. When the Mo-plate reached a temperature of 300 °C the UV-sensitive foil turned red because of the IR-radiation from the hot plate. Therefore the temperature was monitored continuously and kept well below the critical point (230°C < T < 260°C).

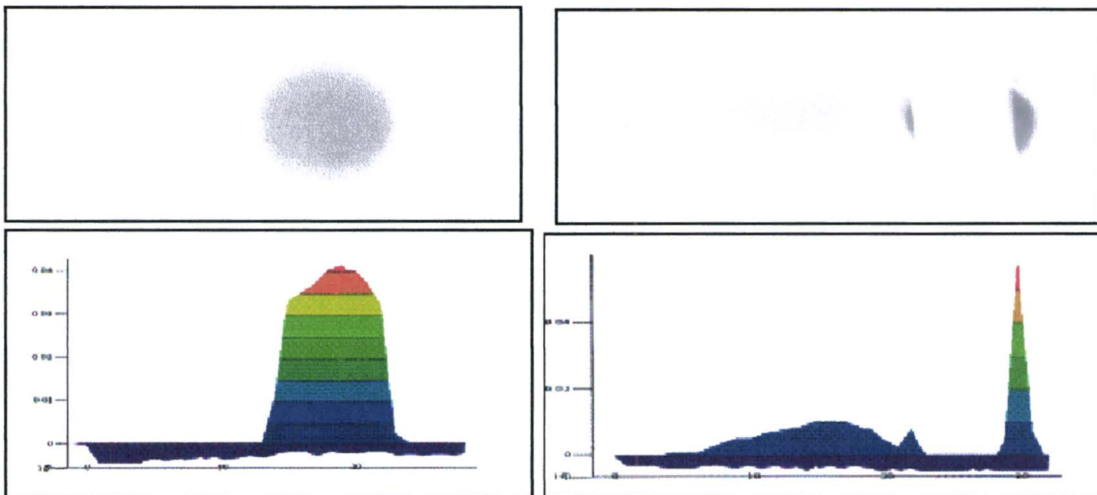

Figure 4.2.2 The two images at the top are from a scan of the UV-sensitive foil and the bottom images are sideviews from the calculated intensity by Mathcad. Left: The image of the pinhole used as reference I_{bb}. Right:The image of the pinhole is partly blocked by the Mo-plate. The broad area on the left is the reflected light I_{cc} , the two pikes at the right are from the non-reflected light I_{aa}

Table 4.2.1 Overview of the experiments together with a calculated reflection coefficient for given roughness [27].

Mo-plate (room temperature)				
Sample nr	alpha [°]	Reflectivity	Theory	Roughness [nm]
041007-3	3	0.10	0.10	57
Mo-plate (room temperature)				**Sn-coated**
Sample nr	alpha [°]	Reflectivity	Theory	Roughness [nm]
041013-2	8	0.29	0.29	5
041014-1	7	0.32	0.35	5
041014-4	6	0.31	0.42	5
041014-3	5	0.56	0.51	5
Hot Mo-plate 230 C < T < 260 C				**Sn-coated**
Sample nr	alpha [°]	Reflectivity	Theory	Roughness [nm]
041015-1	6	0.39	0.42	5
041015-2	6	0.43	0.42	5
Reflectivity = intensity calculated with Mathcad				
Theory = theoretical reflection @13.5nm for given roughness				

Table 4.2.2 Influence of the roughness on the theoretical reflectivity coefficient for a mirror placed at a fixed angle alpha [27].

	Theory		
	alpha	Reflectivity	Roughness [nm]
Mo	3	0.11	56
		0.10	57
		0.09	58
Sn	6	0.49	4
		0.42	5
		0.35	6

Table 4.2.1 shows that the coating enhances the reflectivity significantly, which means that diffuse reflection has been minimized. The surface roughness of a Mo-plate has been measured with an Atomic Force Microscope (AFM) and was found to be 70-80 nm [34]. The fitted surface roughness from the uncoated Mo-plate is of the same order. However, AFM measurements of the Sn-coated Mo-plate showed large irregularities and couldn't confirm the fitted surface roughness.

The heating of the coated plate during the reflectivity experiment has a small effect, but this can be caused by measurement uncertainties as well. The temperature should be raised more to ensure the Sn is liquefied but that was not possible because of the IR-radiation from the hot Mo-plate. The IR-radiation made the chemical substance on the UV-sensitive foil dissolve and thus it was unable to detect UV-light. Figure 4.2.3 shows the measured reflectivity coefficients for the coated Mo-plate together with the error bars.

The red line is the calculated reflection coefficient for a surface roughness of 5 nm. The measurements show a good agreement with the theoretical predicted coefficients.

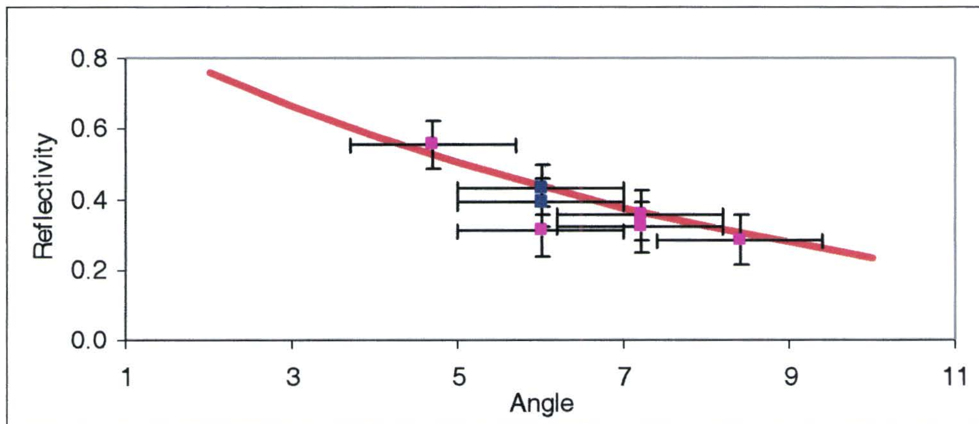

Figure 4.2.3 The measured reflectivity coefficients of a Sn-coated Mo-plate as a function of the angle of incidence. The error for each measurement is also shown. The red line is the calculated reflection coefficient for a surface roughness of 5 nm.

Next a particle mitigation experiment was performed. This means we want to know if the particles stick to the Mo-plate or if they bounce off. The same setup was used, without the Nb-filter and with a Si-sample instead of the UV-sensitive foil. Due to the difficulty of aligning the Mo-plate in front of the pinhole it was impossible to distinguish between the deflected particles and the image of the pinhole. A smaller pinhole could be an option, but this means a smaller droplet transmission and thus a longer exposure time. The longer exposure time would mean a replacement of the laser spot due to erosion of the anode, and thus a replacement of the pinhole image. Then the same problem to distinguish between deflected particles and pinhole image rises again. An alternative setup using a stationary foil trap is described in the following section.

4.2.2 Particle mitigation experiment

4.2.2.1 Introduction

The *reflective foil trap* will be designed to stop the micro-particles. Instead of building a reflective foil trap, a stationary foil trap structure with parallel foils is used. Because the EUV reflection is not important in this experiment, there is no need for using Sn-coated foils. Before performing the experiment, the transmission of droplets through the sta foil trap is estimated.

The transmission is calculated using a two dimensional point source model (PSM) where the foils and the traces of the droplets from the plasma towards the foils are in a single plane **[35]**. The plasma is considered to be a point source. The foils are assumed to be thin relative to the mutual distance b between the foils.
A foil trap of length L is placed at a distance Z_{in} from the pinch with the central pair of foils (slit nr. 0) centered around the optical axis, as shown in figure 4.2.4. Droplets between the blue and green arrows transmit through the slit, while droplets between the green and red arrows are blocked by the foil. The transmission of slit n is then given by

$$T_n = \frac{\beta_n}{\gamma_n} \qquad (4.2.2)$$

with β_n and γ_n respectively the angle of transmission and the angle of entrance in slit n. Both angles are small and thus the use of equation 4.2.2 will be correct. Expressions for β_n and γ_n are given in appendix C.

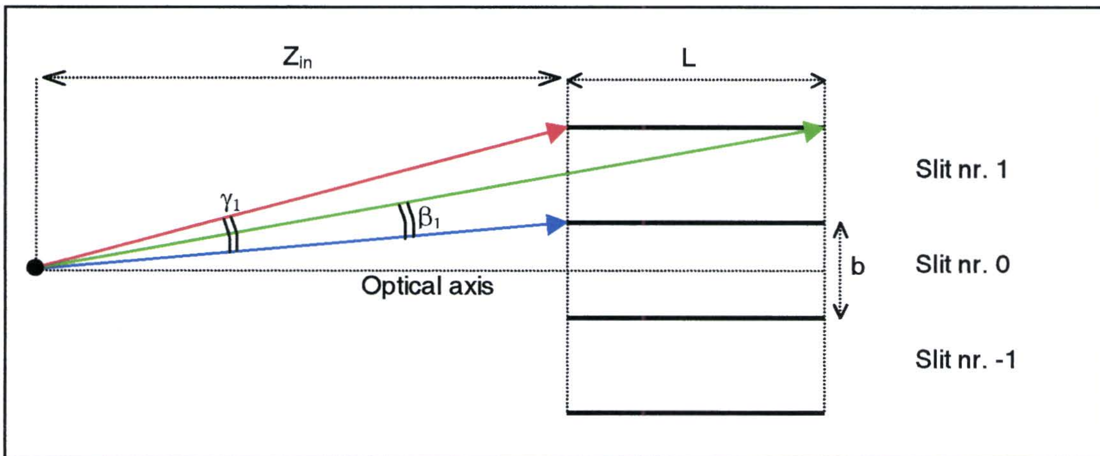

Figure 4.2.4 Schematic of the point source model used to estimate the transmission of the foil trap for the droplets. The foil trap of length L is placed at a distance Z_{in} from the pinch. The foil spacing is equal to b. Droplets between the blue and green arrows transmit through the slit, while droplets between the green and red arrows are blocked by the foil.

The stopping of droplets by a foil trap with parallel foils at a mutual distance of $b = 1$mm and a length of $L = 20$ mm for various Z_{in} is shown in figure 4.2.5. It can be observed that

- The transmission of droplets decreases with decreasing distance between the pinch and the entrance facet of the foil trap.
- The number of pairs of foils having a zero transmission of droplets increases with decreasing distance between the pinch and the entrance facet of the foil trap.

The impact of longer foils on the transmission is shown in figure 4.2.6. The longer foils result in a reduction of the number of foils having a nonzero transmission.

In practice the foils will not be perfectly aligned with respect to the optical axis. They have an offset with respect to the optical axis. This gives rise to a shifted droplet transmission curve, which has to be taken into account when comparing the experimental values with the theoretical calculated transmission.

There is one major deficit of this point source model: the origin of the debris isn't from one infinitely small point. The plasma of the discharge has a growing width during the discharge with a medium width of about 2 mm [9]. The origin of the particulate debris is therefore expected to come from a larger area.

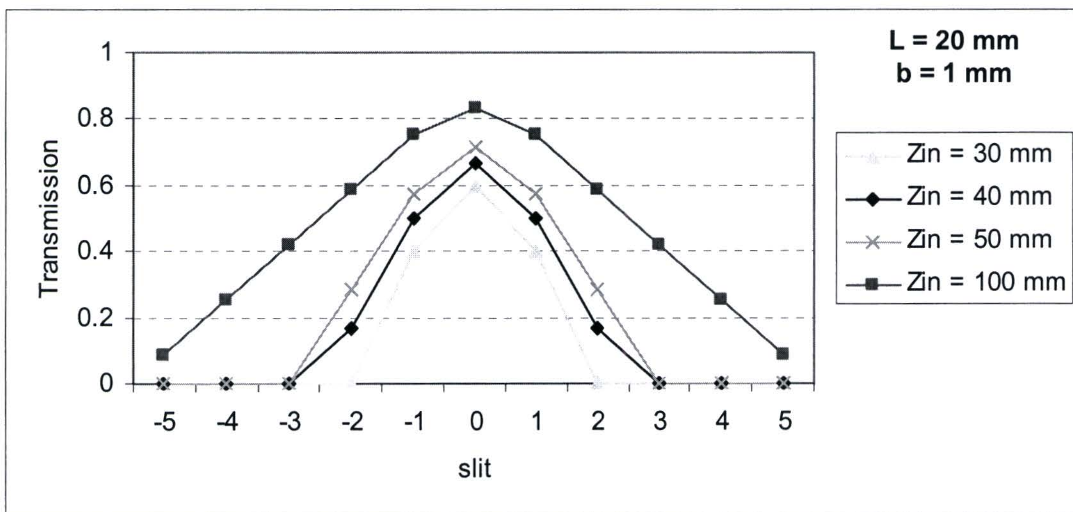

Figure 4.2.5 Transmission of droplets with the distance between the pinch and the entrance facets of a foil trap with parallel foils as parameter with L = 20 mm and b = 1 mm. The central pair of foils (slit 0) is centered around the optical axis.

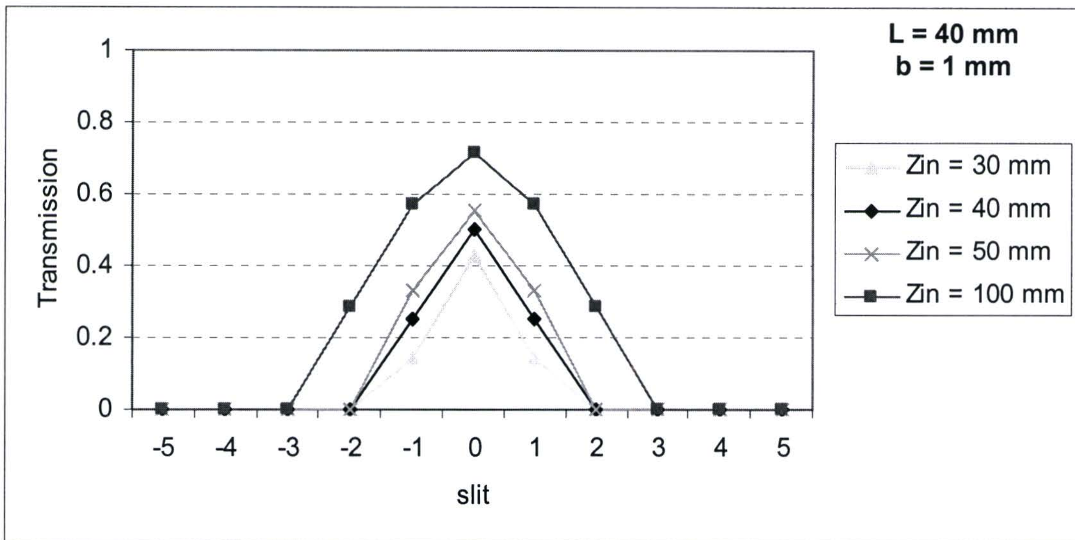

Figure 4.2.6 Transmission of droplets with the distance between the pinch and the entrance facets of a foil trap with parallel foils as parameter with L = 40mm and b = 1 mm. The central pair of foils (slit 0) is centered around the optical axis.

The transmission will now be calculated using an extended point source model (EPSM). In this 2 D model the origin of the droplets is considered to be from three point sources, two at the ends and one in the center of the width of the pinch. The three point sources are considered to have the same droplet emission intensity and the transmission of the foil trap for each point source is described using the 2 D PSM. Then the transmission coefficients are added up for each slit and normalized to the center slit. For the case of Z_{in} = 40 mm, L = 20 mm and b = 1 mm the PSM and the EPSM transmission curves, all normalized to the transmission of the center slit, are plotted in figure 4.2.7. The EPSM has been plotted for width w = 2.0 mm, w = 3.0 mm and w = 4.0 mm to see the impact of the width of the origin of the particles on the transmission. It can be observed that

- The transmission for each slit increases with increasing width w in the EPSM
- The number of slits having nonzero droplet transmission increases with increasing width w in the EPSM.
- There can be more slits with maximal droplet transmission

It has been shown that with a static foil trap structure, there are always some slits with nonzero droplet transmission. By varying the distance between the pinch and the entrance of the foil trap, one can increase/reduce the number of foils with nonzero droplet transmission.

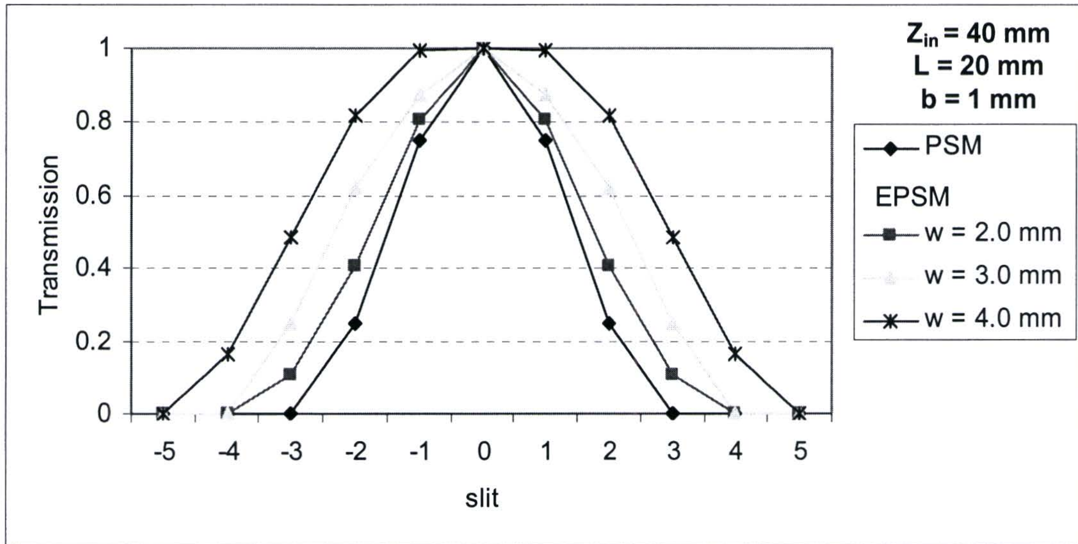

Figure 4.2.7 Transmission of droplets for the PSM and EPSM with parameters Z_{in} = 40 mm, L = 20 mm and b = 1 mm. The 2 D model is plotted for a discharge of width w = 2.0 mm, w = 3.0 mm and w = 4.0 mm. The transmission is normalized to the transmission of the center slit.

4.2.2.2 Experiment

The static foil trap used in the experiment has an aperture size measuring 20 × 10 mm, a length of $L = 20$ mm and a spacing of 1mm between the foils and was placed at a distance of $Z_{in} = 41$ mm from the source. A Si-sample with the same dimensions as the aperture size was placed directly behind the foil trap. The pressure in the vacuum chamber was 2×10^{-5} mbar and the sample was exposed to about 200 kshot. The experimental setup is shown in figure 4.2.8.

Pictures of magnification 5 ×, taken with an optical microscope, are shown in figure 4.2.9. On each picture the shadow of a foil is visible and the slits are numbered beginning from the left-hand side. It is clearly seen that slit nr. 3 has the highest coverage of droplets and slit nr. 9 wasn't exposed.

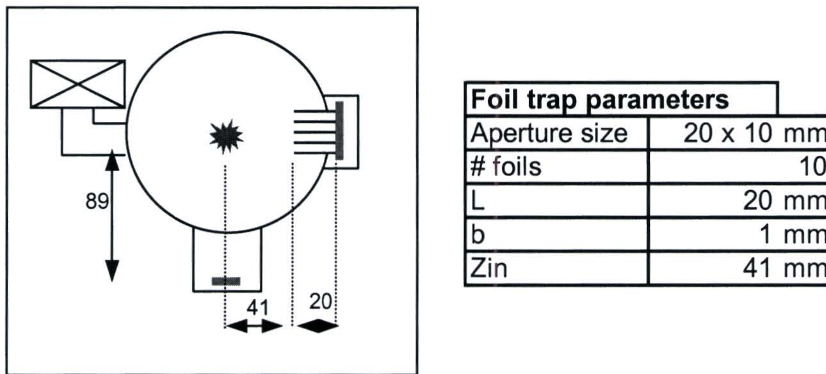

Foil trap parameters	
Aperture size	20 x 10 mm
# foils	10
L	20 mm
b	1 mm
Zin	41 mm

Figure 4.2.8 Setup of the experiment and parameters of the foil trap used to test the particle mitigation. Behind the foil trap a Si-sample of 20 × 10 mm was placed and a reference sample was placed at 89 mm from the pinch.

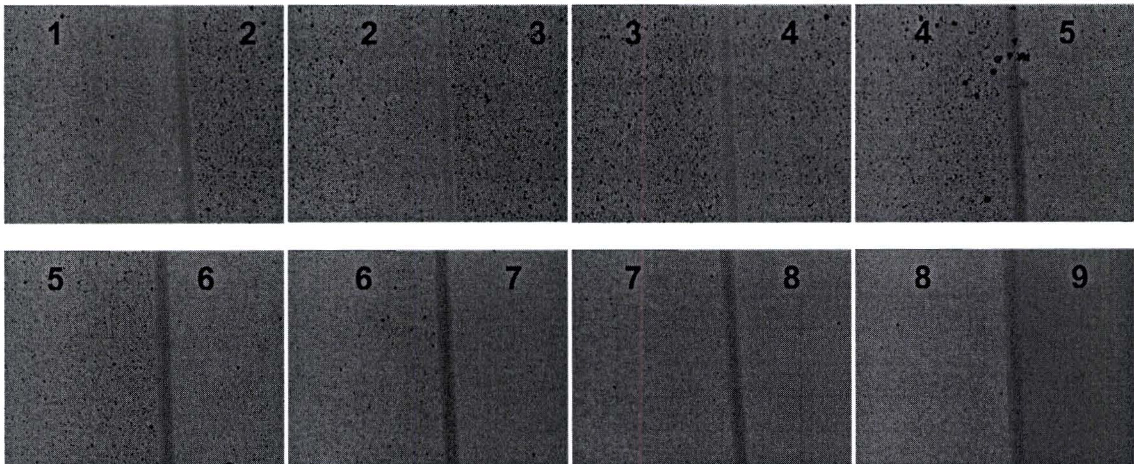

Figure 4.2.9 Pictures of the Si-sample taken with an optical microscope (5×). The pictures are taken in such a way that the shadow of a foil is visible; the numbers indicate the slit number.

The coverage ratio for droplets in each slit was determined using the ISAN software for optical images (20×) and SEM images (500×), taken on the right-hand side of each slit. The coverage ratio has a 10% error for each picture. The coverage of the reference sample was recalculated to a distance of 41 mm and then the transmission of each slit was calculated using the following formula and then normalized to slit nr.3.

$$T_n = \frac{coverage\ slit\ n}{coverage\ reference} \tag{4.2.3}$$

Figure 4.2.10 shows the transmission of droplets from the 20x and 500x images together with the EPS model. The error of 10% on the measured coverage value is indicated with the error bars. For the EPS model the best fit was found for a width w = 2.5mm and an offset of 0.5 mm with respect to the center of slit nr.3.

There is an excellent match between the EPS model and the transmission calculated from the 20x images. The transmission calculated from the 500× images show some irregularities. With this magnification a small change in position may cause a great change in droplet coverage as seen in slit 5. The droplet coverage for slit 7 and 8 is near the background dust level, which is fairly high for the optical microscope.

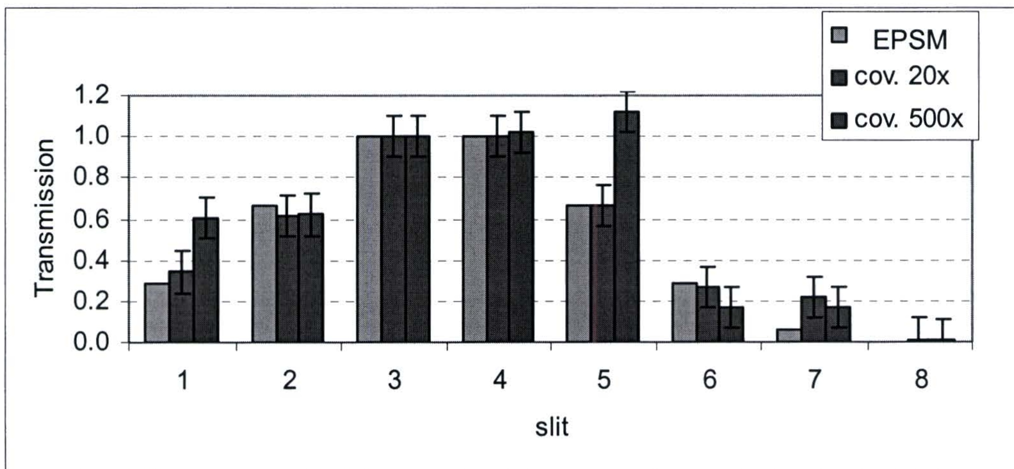

Figure 4.2.10 The transmission of droplets from the 20× and 500× images together with the EPS model. The width of the origin of droplets is fitted to be 2.5 mm and the center has an offset of 0.5 mm with respect to the center of slit 3. The bars show the transmission error based on the 10% of the droplet coverage.

4.3 Gas controlled stationary foil trap

Until now the stationary foil trap (SFT) has been used in combination with the RFT to increase the suppression of particulate debris and as a tool to test the particle mitigation of the reflective foil trap. In those experiments the mitigation of the particulate debris was controlled by the geometry of the SFT.

In order to stop the atomic-ionic debris a SFT will be inserted with an Ar buffer gas. Whenever the atom or ion hits the surface of one of the foils, it sticks there and thus is trapped inside the foil trap. Increasing the pressure of the buffer gas will increase the probability that an atom hits one of the walls. The buffer gas has to be as transparent as possible for EUV photons leaving the plasma.

Collisions of atomic-ionic debris with the buffer gas atoms form an essential part of the foil trap principle, so it is important to understand the dynamics of gas collisions. The cross-section and mean free path of Sn-atoms in a background Ar gas will be discussed first. Then the working principle of the gas controlled SFT is described using two different models, depending on the relation between the mean free path and foil spacing. For each model an expression for the suppression of debris is found. Finally a debris mitigation experiment has been performed and compared to the different models.

4.3.1 Cross-section and mean free path

Cross-section σ

In the case that the debris is electrically neutral a hard sphere model would be sufficient. Neutral particles only interact noticeably at short distances to each other and the interaction is approximated by a hard sphere interaction. In hard sphere collisions, the particles are represented by spheres with well-defined radii and masses. These particles only interact if they actually touch each other. The collision cross-section σ is defined as πd^2, where $d=r+R$ is the distance between two particles with radii r and R. The collisions are assumed to be elastic so no kinetic energy is lost during the collision.

Real atoms are of course no hard spheres, but the hard sphere potential is a reasonable approximation. Two real atoms will interact even at very large distances, the potential extents to infinity. This is called the Coulomb interaction. The atom not only interacts with one atom but with all atoms, which are within the reach of the Coulomb interaction. It is difficult to find values for this cross-section in literature. Mostly the values are given for thermalized particles. Cross sections for high-energy particles will deviate significantly from these values because for different energies different cross-sections are found. Cross-sections for slow and fast atomic Sn debris in an Ar background gas have

been experimentally determined at ISAN. The values found are for slow debris $\sigma = 2 \times 10^{-19}$ m^2 and for fast debris $\sigma = 2 \times 10^{-20}$ m^2.

Mean free path λ

The mean free path determines how often collisions occur. The average frequency at which these collisions occur is the mean collision frequency f_c. We consider a test particle with velocity v that is moving in a field of background particles, all moving in the same direction with velocity v_b. We choose a frame of reference in which the background particles are all stationary and the test particle moves at velocity $v_r = v - v_b$ relative to the background particles. (fig 4.3.1)

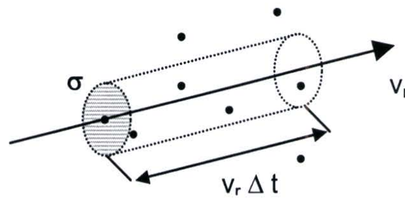

Figure 4.3.1 Particle with cross section σ moving through field of background particles.

The volume swept by the test particle per unit of time is equal to the collision cross-section times the distance traveled per unit of time. The number density n of the background particles times this volume gives the average number of collisions per unit of time

$$f_c = n \cdot \sigma \cdot v_r \tag{4.3.1}$$

The mean free path for collisions λ_c is the average distance traveled by a particle with velocity v between two successive collisions and is given by

$$\lambda_c = \frac{v}{f_c} = \frac{v}{v_r}\frac{1}{n \cdot \sigma} \tag{4.3.2}$$

when v is much larger than the velocity of the background particles, then the relative speed is equal to v. The equation for the mean free path is now independent of the test particle velocity and expressed only in function of particle density and cross-section, but there is still a dependence of σ on v.

$$\lambda = \frac{1}{n \cdot \sigma} \tag{4.3.3}$$

The number density n of the background particles is easily calculated with the following formula

$$p = nkT \quad (4.3.4)$$

where p is the pressure, k the Boltzmann number and T the temperature.

4.3.2 The gas controlled SFT principle

The foil trap consists of ten equally spaced thin Mo foils with length L, and spacing b, arranged in the propagation direction of the EUV photons. (fig 4.3.2) Whenever an atom or particulate hits the surface of one of the foils it sticks and thus is trapped inside the foil trap.

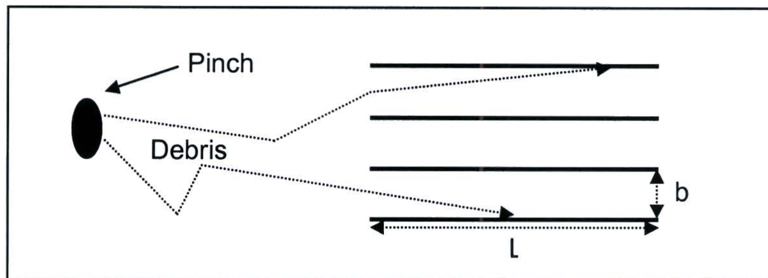

Figure 4.3.2 The foil trap principle and geometry. The foils have length L and spacing b.

At low pressure the mean free path is much greater then the foil spacing and length. The geometry of the foil trap and the direction of the debris determine if an atom will hit one of the walls. When the pressure increases, the mean free path becomes smaller and the probability that the debris will hit one of the walls will increase due to collisions of the debris with the buffer gas atoms. For high pressures, the number of collisions needed to reach either the exit or one of the walls, will increase dramatically. The buffer gas can now be treated as a continuous medium and the movement of the debris can be described as a diffusion process.

The trajectory of the EUV photons is unaffected by the presence of the buffer gas, although there is a small loss of photons due to absorption by the gas atoms. By making the buffer gas region as small as possible and by choosing a relatively transparent buffer gas like argon this loss can be kept to a minimum. Also the buffer gas pressure should not be higher than strictly necessary.

The working principle of the foil trap can be described by three different models, all for the case that the foil spacing is smaller then the foil length ($b \ll L$).

1. Beam extinction model [36] ($\lambda >> b$)
2. Anisotropic diffusion model ($\lambda \approx b$)
3. Diffusion model [36] ($\lambda << b$)

Figure 4.3.3 shows that the suppression of the fast debris, with smaller cross-section, has to be calculated using the beam extinction model whereas for the slow debris, with greater cross-section, the anisotropic diffusion model has to be used. These models will be explained in the next chapter. The diffusion model will not be treated here. The reason is that it does not lead to a practical solution since high pressure in the foil trap implies that it is too difficult to maintain a sufficient low pressure at the pinch.

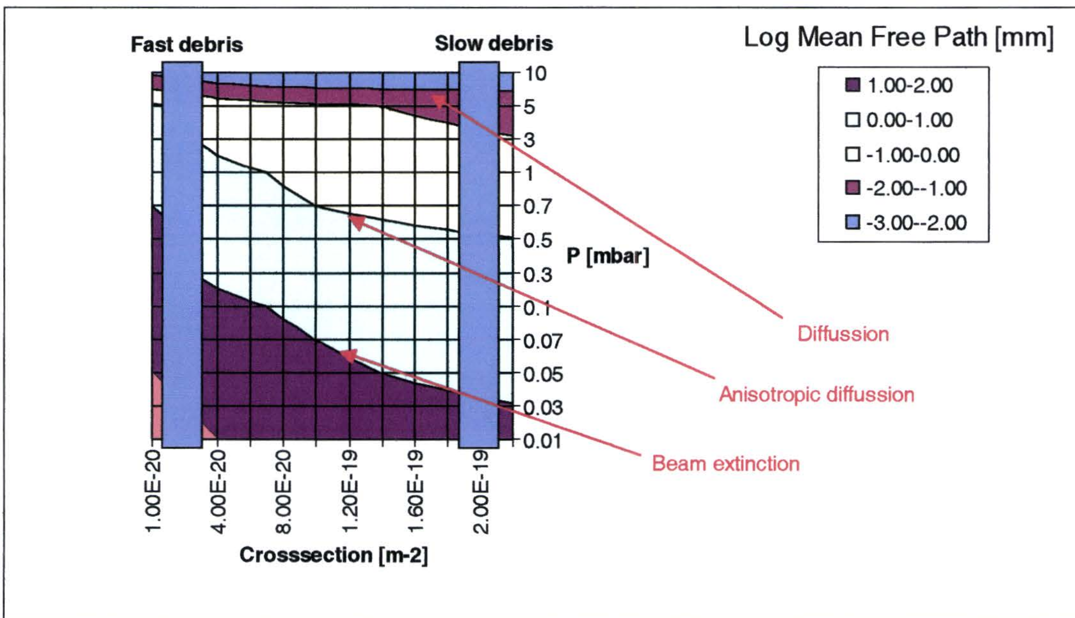

Figure 4.3.3 A logarithmic scale of the mean free path as a function of the cross-section σ and the pressure p. The two rectangular boxes indicate the mean free path in case of the fast and slow debris. The arrows indicate the cross-over lines for which different models have to be used for b = 1 mm.

4.3.2.1 Beam extinction model ($b << \lambda$ and $b << L$)

If the foil trap is long and narrow and the pressure is very low, the particles traveling in the right direction to reach the exit form a narrow beam. All other particles will hit the foil almost immediately. When the pressure is raised the chance of a gas collision increases. When a particle in the beam collides, it is almost instantly lost. The chance that this particle still has the right direction to reach the exit is very small because $b << L$, and the chance that the particle gets a second chance to collide back into the beam before it hits the wall is also very small because $b << \lambda$. There will be some particles outside the beam that deflect into the beam and reach the exit, but this will only be a very small fraction of all the particles. Almost all particles outside the beam will hit the wall within a few times b and will not get a chance to collide.

So only a fraction of particles that is in the beam and does not collide, will exit the foil trap. The fraction of particles that has not collided after a distance x is given by $\exp(-x/\lambda)$, so the transmission of the foil trap is given by

$$T_r = G \exp\left(-\frac{L}{\lambda}\right) \tag{4.3.5}$$

where G is a function of geometry and equals b/L for $b<<L$. This equation together with eq.4.3.3 and eq 4.3.4 gives the expression for the suppression of the foil trap.

$$SUP = \frac{1}{T_r} = \frac{L}{b} \exp\left(L \cdot p \frac{\sigma}{k \cdot T}\right) \tag{4.3.6}$$

Figure 4.3.4 shows the suppression rate of the fast ionic-atomic debris by a SFT in function of the parameters.

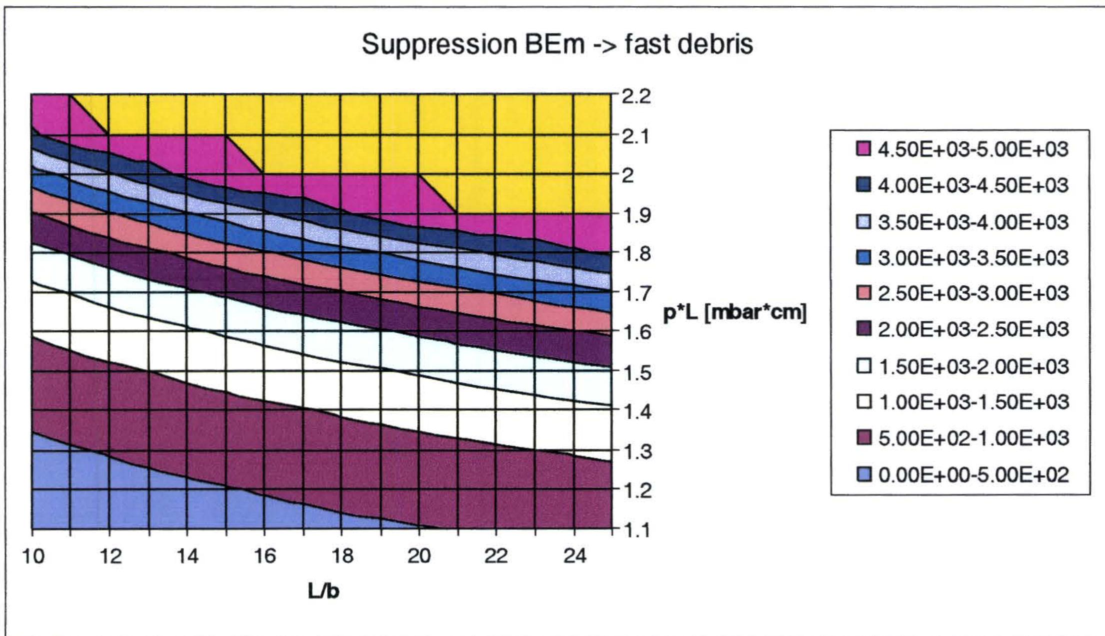

Figure 4.3.4 The suppression rate of the fast ionic-atomic debris by an SFT with length L, spacing b and injected with an Ar-gas pressure p in the Beam Extinction model.

4.3.2.2 Anisotropic diffusion model ($\lambda \approx b << L$)

When the mean free path is in the order of the foil spacing ($\lambda \approx$ b) and b << L, then the number of collisions that a particle will suffer in its path along the foils will be very large. The particle movement has to be treated with the Anisotropic diffusion model. That means that the transport in the direction parallel to the foils (x-direction) can be described with diffusion; while movement in the y-direction is a molecular flow, which depends on the thermal velocity of the atoms. The idea is that particles will be removed due to a quasi-free motion in the y-direction towards the foils. This leads to a decrease in the density in the x-direction. Such a non-uniformity will invoke diffusion. In order to find an expression for the suppression of the foil trap, a differential equation of the number density n has to be solved.

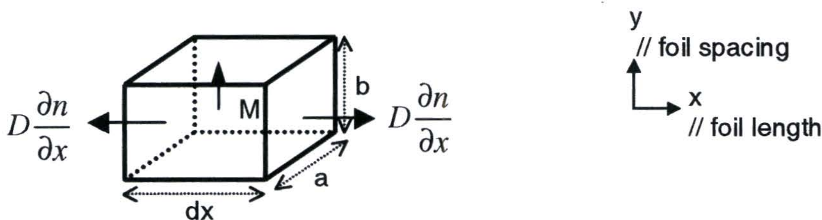

Figure 4.3.5 Particles will be removed due to a quasi-free motion in the y-direction (M) towards the foils. This leads to a decrease in the density in the x-direction. Such a non-uniformity will invoke diffusion.

Consider a volume between two foils with length dx, width a and height b (fig 4.3.5). Particles will be removed out of the volume by a molecular flow in the y-direction. The diffusion flow in the x-direction tries to compensate for this loss in density. The number density n of the particles inside this volume can be written as

$$D\left[\left(\frac{\partial n}{\partial x}\right)_{x+dx}-\left(\frac{\partial n}{\partial x}\right)_{x}\right]b\cdot a=M\cdot a\cdot dx \qquad (4.3.7)$$

The molecular flow M can be expressed as

$$M=2\frac{n\cdot v_{th}}{4} \qquad (4.3.8)$$

with v_{th} the thermal velocity of the debris. The factor 2 was added to the equation because the flow is both upwards and downwards. Rewriting equation 4.3.7 and using equation 4.3.8 gives the differential equation for anisotropic diffusion.

$$D\frac{\partial^2 n}{\partial x^2}=\frac{v_{th}}{2b}n \qquad (4.3.9)$$

The diffusion coefficient D can be expressed as

$$D=\frac{\lambda\cdot v_{th}}{3} \qquad (4.3.10)$$

Solving the differential equation and using equations 4.3.3 and 4.3.4 and 4.3.10 gives the following formula for the suppression

$$SUP=\exp\left[\sqrt{\frac{3}{2}\frac{\sigma}{kT}}\cdot\sqrt{\frac{p}{b}}\cdot L\right] \qquad (4.3.11)$$

Figure 4.3.6 shows the suppression rate of the slow ionic-atomic debris by a SFT in function of the parameters.

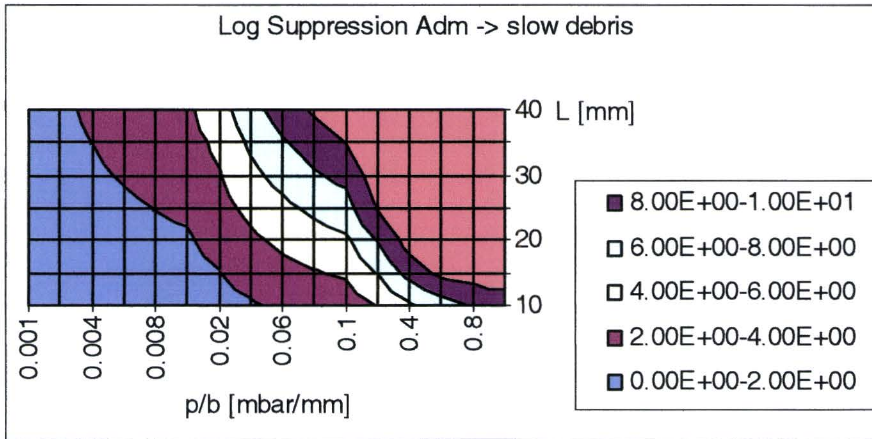

Figure 4.3.6 A logarithmic scale of the suppression rate of the slow ionic-atomic debris by an SFT with length L, spacing b and injected with an Ar-gas pressure p in the Anisotropic diffusion model.

4.3.3 Experiment

When performing experiments to measure the amount of atomic debris it has to be taken into account that together with the debris a lot of micro-particles are deposited on the detection device as well. This means that without mitigation of droplets it is difficult to determine an absolute value for the atomic debris. Figure 4.3.7 shows the experimental setup. Because we are interested here in the total amount of (slow) atomic debris and want to trace the deposition of debris during the exposure, a Quartz Crystal Microbalance (QCM) further explained in appendix A, was used for measuring the mass of deposited debris. Finally the experimental measured suppression of debris was compared with the theoretical models explained above.

First a Si-sample was placed at 160 mm from the pinch, next to QCM2, to check if the Ar gas has any influence on the droplet formation as seen in the RFT experiment performed with the Philips-source. Two samples were exposed to 40 kshot: one under vacuum conditions (5×10^{-5} mbar) and one with a Ar-gas pressure of 5×10^{-3} mbar. The coverage of the samples was respectively 0.54 % and 1.09 %. Again an increase in the amount of droplets is seen, caused by the presence of the Ar-gas. As shown in section 4.1 the extra droplets do not form any problem for mitigation with the RFT.

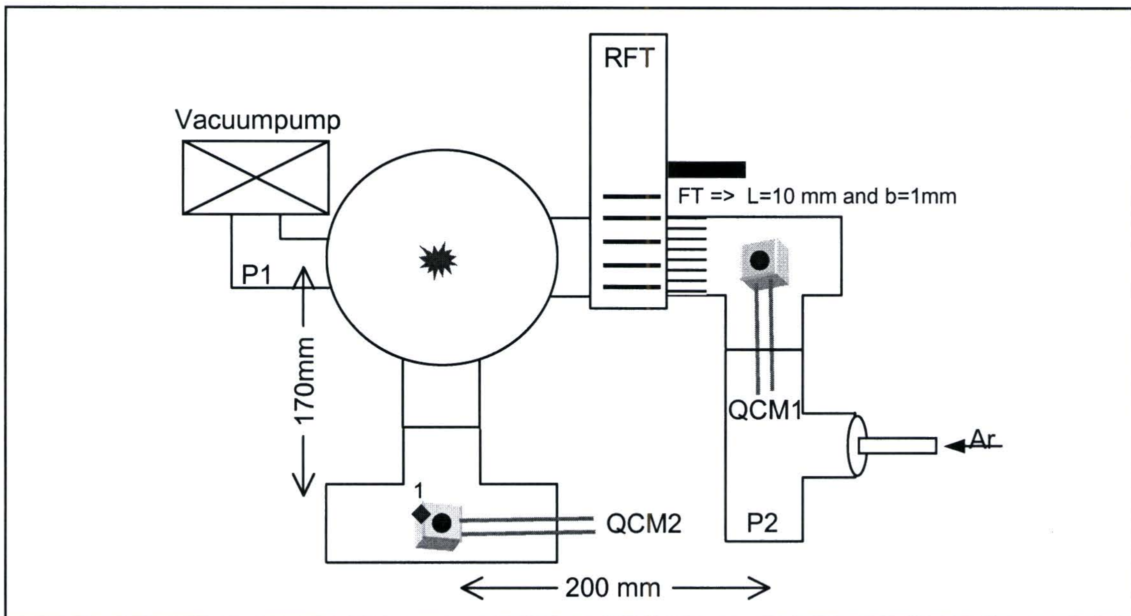

Figure 4.3.7 Experimental setup for determining suppression of atomic debris by the foil trap (FT) injected with Ar-gas. The arrow on the right shows the inlet of the Ar-gas. Two QCM's were used for determining the amount of debris. P1 and P2 indicate the locations where the pressure was measured. A Si-sample (1) was placed at a distance of 160 mm from the source to see if the Ar has any effect on the droplet formation.

The QCM was placed behind the rotating foil trap (RFT) and static foil trap (SFT). The frequency of the RFT was 75 Hz and so all the particles up to a speed of 640 m/s were stopped. No noticeable droplets will reach the QCM and disturb the measurement. The foil trap structure had a length of L = 1 cm and spacing between the foils b = 1 mm. For determining the suppression of atomic debris by the foil trap and also for monitoring changes in the amount of debris generated by the Sn-source a second QCM was used, directly facing the source at a distance similar to the QCM behind the static foil trap.

Figure 4.3.8a shows the experimental results obtained from QCM1 for different Ar-pressures while on fig 4.3.8b it can be clearly seen that during the experiment the total amount of deposited debris did not change significantly. This means that the decrease in the deposition rate on QCM1, is due to suppression of atomic debris in the FT.

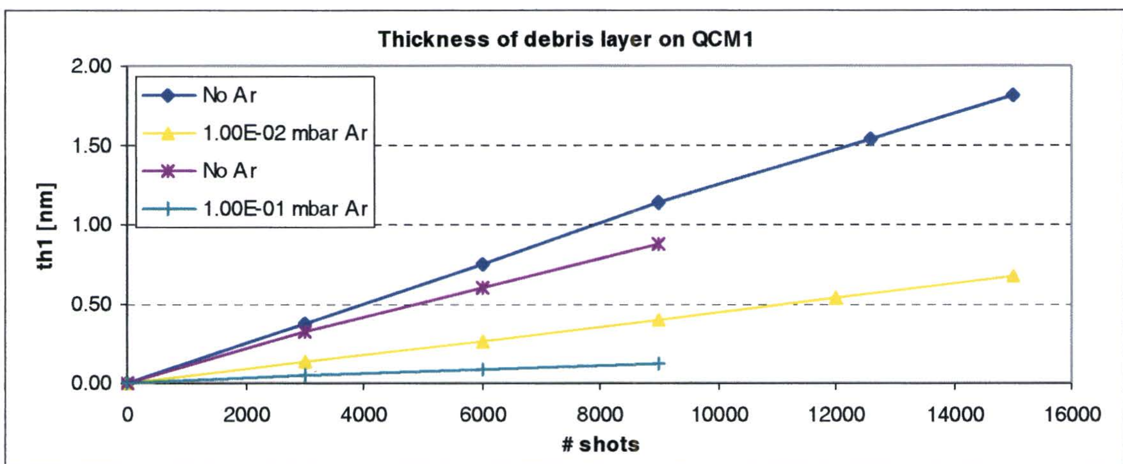

Figure 4.3.8a The thickness of the debris layer on QCM1 for different pressures, measured at P2. At higher pressures the deposition rate of the atomic debris slows down which means that there is suppression of atomic debris inside the FT.

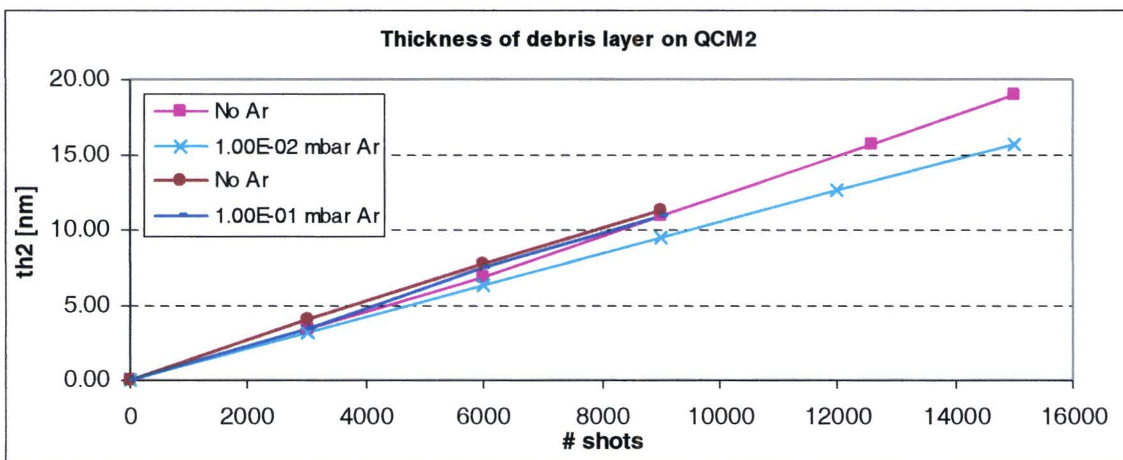

Figure 4.3.8b The thickness of the debris layer on QCM2 for different pressures measured at P2. The different Ar pressures have no influence on the deposition rate of the debris.

Table 4.3.1 Summary of the measured values for the deposition rates of debris at QCM1 and QCM2 for different Ar-pressures. The measured deposition rates for QCM2 are corrected for the difference in distances between QCM1 and QCM2 from the source and for the amount of droplets on QCM2. The resulting suppression of atomic debris is shown in the last column.

Ar	P1 [mbar]	P2 [mbar]	QCM1 [nm/Mshot	QCM2 [nm/Mshot	SUP
No	1.00E-04	2.00E-04	121	458	3.8
Yes	1.00E-03	1.00E-02	45	378	8.4
No	2.00E-04	5.00E-04	98	454	4.6
Yes	1.00E-02	1.00E-01	13	438	33.7

From the curves of fig 4.3.8 the amount of deposited debris per Mshot is calculated. The results for QCM2 are corrected for the difference in the distances between QCM1 and QCM2 from the source and it is taken into account that only about 50% of the debris on QCM2 is atomic. The results are summarized in table 4.3.1. The last column shows the suppression of atomic debris by the foil trap. The suppression at a pressure of 0.1mbar at the inlet is a factor of 33 with a foil trap of 1 cm length. This is a factor of 7 better than the suppression of atomic debris in the case of no Ar gas at the inlet.

Table 4.3.2 shows the suppression rates of the experiment in comparison with the theoretical suppression models. From figure 4.3.3 it can be seen that the Beam extinction model should be used at this low pressure inside the FT. The beam extinction model however, has a lower limit given by L/b, which is 10 for our setup, and is only valid for b << L. The foil length L is not long enough to use this model here, so the anisotropic diffusion model will be better for the lower pressures. The pressure measured at P2 is used in the models except in the last row. Here the pressure in the FT is fitted so the calculated suppression is in the order of the experimental value. It can seen that the pressure inside the FT is a factor of 5 lower than measured at P2.

Table 4.3.2: The suppression rate of the FT at different pressures as measured with the QCM and calculated with the anisotropic diffusion model (Adm) and beam extinction model (Be) for T=300K and $\sigma = 2x10^{-19}$ m^2. The pressures used in the models are also given.

Ar	P1 [mbar]	P2 [mbar]	Exp SUP	Adm SUP	Adm P [mbar]	Be SUP	Be P [mbar]
No	1.00E-04	2.00E-04	3.8	1.5	2.00E-04	10.1	2.00E-04
No	5.00E-04	2.00E-04	4.6	1.5	2.00E-04	10.1	2.00E-04
Yes	1.00E-03	1.00E-02	8.4	14.8	1.00E-02	16.2	1.00E-02
Yes	1.00E-02	1.00E-01	33.7	4976.9	1.00E-01	1253.3	1.00E-01
Yes	1.00E-02	1.00E-01	33.7	33.4	1.70E-02	33.5	2.50E-02

5. Discussion

In this chapter some problems encountered during the experiments and the effect of the mitigation schemes on the collector mirror lifetime will be discussed. We will start with the effect of the erosion of the electrodes on the experimental results. Next the lifetime of the collector mirror as a function of the stopping speed of the particulate debris will be calculated. Finally with the use of the two suppression models from section 4.3, the pressure in the gas controlled stationary foil trap (SFT) that is needed to fulfill the lifetime demands of the collector mirror will be estimated.

Erosion of the electrodes

While measuring the fast ionic-atomic debris no significant erosion of the electrodes was observed. The experiments with the faraday cup were of short duration and thus the results from these experiments are gathered with constant laser pulse intensity for an anode-cathode distance of about 3 mm.

However when performing experiments which were of a long duration, the erosion of the anode and cathode increased the electrode gap distance as seen on figure 5.1. In order to prevent a destabilization of the discharge, the laser position can be moved along the edge of the anode and the laser intensity can be increased.

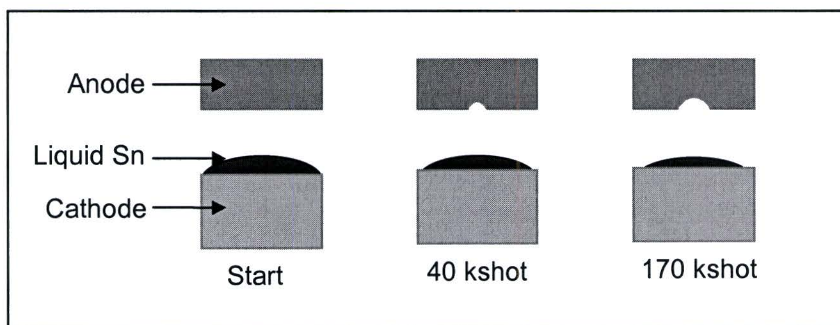

Figure 5.1 The erosion of the anode and cathode because of long duration experiments. After about 40 kshot an erosion of the anode is observed. After about 170 kshot the level of the liquid Sn on the cathode surface has decreased significantly resulting in an increased electrode gap distance.

First, if the anode has eroded but there is still enough Sn on the cathode surface, the laser position can be moved along the anode edge. This means that the position of the discharge plasma has been changed as well. For most experiments this was no problem except for the experiments concerning the particle mitigation of the reflective foil trap. During this experiment with the SFT, the sample had been exposed to about 200 kshot and the position of the laser had to be slightly moved to ensure a stable discharge. The width of the origin of the particle debris can thus be smaller than the fitted value of 2.5 mm for the Extended Point Source model of section 4.2.2.

After about 170 kshot, the level of the liquid Sn on the cathode surface has decreased significantly resulting in an increased electrode gap distance. In this case a movement of the laser position has no effect on the stabilization of the discharge. However increasing the laser pulse energy does. This can be explained by the increased amount of ablated material when a larger pulse energy is applied: first contact of the vapour with the anode, which was delayed because of the decreased Sn-level at the cathode surface, will be reached faster again and the larger amount of material stabilizes the discharge through the increased electrode gap distance.

The effect of the laser pulse energy on the production of debris is difficult to determine. For a certain anode-cathode distance there is an optimum value for the laser pulse energy. This means that increasing the laser pulse energy without an increased electrode gap distance will destabilize the discharge and disturb the experiment. In order to measure the effect of the laser pulse energy on the production of the particulate and slow atomic debris, long time experiments are needed and this involves changing the laser pulse energy during the experiment to ensure a stable discharge.

Micro-particles

From the experiments with the rotating foil trap (RFT), performed with the Philips source, it had been found that with a rotation speed of 75 Hz (stopping droplets up to 640 m/s) the droplet coverage was below the background dust level, which had a coverage of 0.01 %. During this experiment the sample was exposed to 4 Mshot. While taking SEM images of the sample we found that the surface coverage by dust particles is larger then the coverage with micro-particles. In order to prove the feasibility of the RFT for a mirror lifetime of 5×10^9 shots with respect to the micro-particles, we need apart from longer exposure times also cleaner samples.

Figure 5.2 shows the lifetime of the collector mirror in function of the stopping speed of the particulate debris. The stopping speed is shown instead of the rotating frequency because a different geometry of a RFT involves a different rotating speed to stop the particles. The data points indicate the lifetime calculated from the coverage ratio's from table 4.1.1 (RFT experiment with a 10 sccm Ar flow, performed at Philips) and multiplied by five to correct for the grazing angle of incidence of the EUV radiation as explained in section 3.3. The gray line shows the background dust level of the samples in the experiment and the black line indicates the trend in the measurements and shows that with a stopping speed of about 650 m/s a lifetime of 5×10^9 (red line) will be reached.

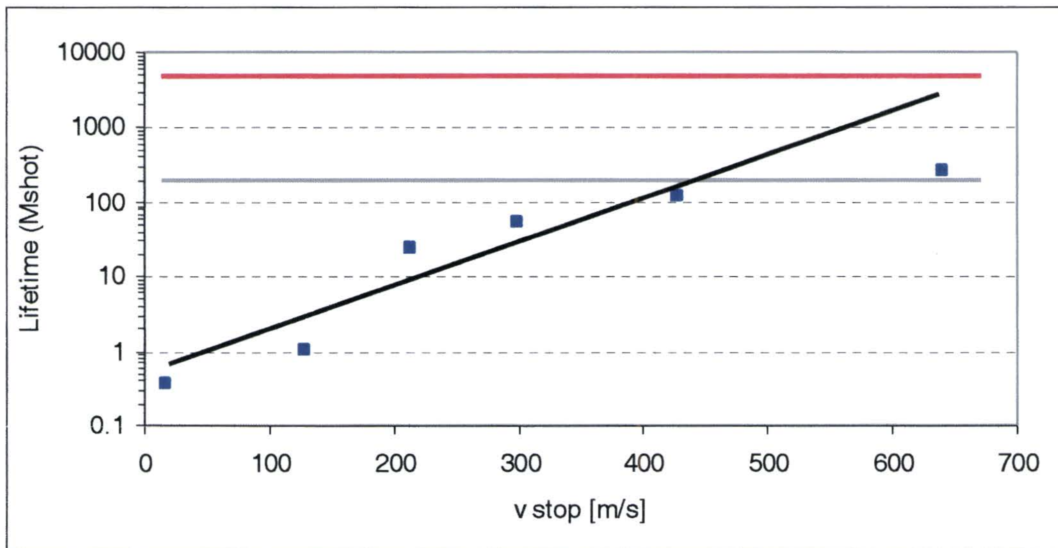

Figure 5.2 The lifetime of the collector mirror in function of the stopping speed of the droplets as calculated from the RFT experiment. The gray line shows the background dust level from the samples used in the experiment and the black line indicates the trend in the data. By extrapolating this trend it is found that with a stopping speed of about 650 m/s a lifetime of 5×10^9 shots (red line) will be reached.

Slow atomic-ionic debris

In section 3.4 the total amount of slow atomic-ionic debris was measured and was found to be equal to 5×10^{15} atoms/shot in a solid angle of 4π directly at the source. The discharge plasma before the pinch has an electron density of 1×10^{24} m^{-3} in a volume of about 1 mm^3. Taking an average ionization degree of $Z = 8$, this means that there are about 1.2×10^{14} atoms present in the discharge plasma. This is a factor of 40 lower than the measured amount of atomic debris!

The extra amount of debris can be explained by the formation of a second, much cooler plasma, formed just after the pinch. This second plasma was observed by the appearance of visible light radiation at the cathode surface after the pinch. Since a similar emission does not appear in the EUV, it must be generated by a much cooler plasma [9]. Heating of the liquid Sn by the current through the pinch plasma and absorption of EUV radiation most likely causes the evaporation and partial ionization of Sn from the cathode. This demonstrates that there is still room for reduction of the debris production by the source, besides mitigation strategies.

In section 4.3 the mitigation of slow atomic-ionic debris by use of an Ar-controlled SFT was demonstrated. The Ar-gas pressure in the setup was measured at the Ar-gas inlet and in the vacuum chamber at the vacuum pump inlet. A comparison of the experimental suppression rate of the debris and the suppression rate calculated with the Anisotropic Diffusion model showed that the pressure inside the SFT should have be 1.7×10^{-2} mbar. This is a factor of 6 lower than measured at the Ar-gas inlet, 1×10^{-1} mbar. The pressure

inside the vacuum chamber during this experiment was found to be 1×10^{-2} mbar. Increasing the Ar-pressure above this point led to destabilization of the discharge and the formation of random discharges through the Ar-gas. This made it impossible to perform experiments with higher Ar-gas pressures inside the SFT and set the maximum suppression rate with this setup to a factor of 33.

Figure 5.3 shows the calculated lifetime of the optics in function of the *pd*-value. The calculation has been done with the use of the Anisotropic diffusion model. The *pd*-value equals to the Ar pressure *p* inside the SFT (expressed in mbar) times the length *L* (expressed in cm) of the SFT. The reason for the use of *pd* is that the suppression of debris can be increased not only by raising the pressure in the SFT but also by increasing the length. The lifetime is defined as how many shots a mirror can have before it loses 10 % of its maximum reflectivity. For a grazing angle of incidence of 10 degrees this corresponds to about a deposited layer of Sn of 1 nm.
The calculation has been done for the case of 10^{15} atoms/shot in a solid angle of 4π directly at the source and with a temperature of the Ar gas of about 500 K (in a newly developed Sn-source the production of atomic debris will be lower and because of an increased repetition rate the temperature of the background gas will be higher). From the figure it can be seen that with a *pd*-value of 2 mbar $\times$ cm, a lifetime of 10^8 shots will be reached (indicated with a green line). In order to reach the goal of 5×10^9 shots (red line) a cleaning strategy will have to be used.

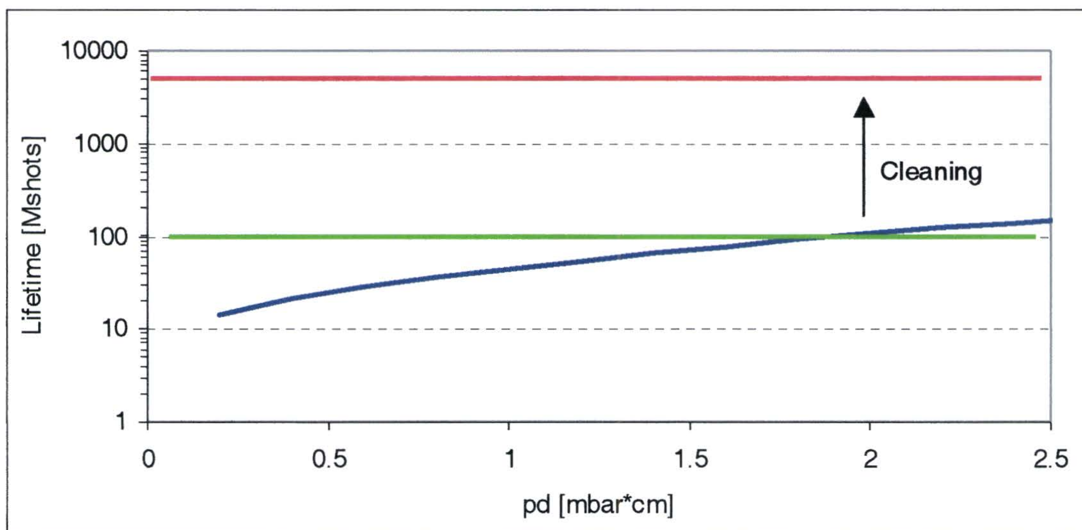

Figure 5.3 Lifetime of the optics as a function of pd, which equals the Ar pressure inside the foil trap times the length L of the foil trap with spacing b = 1 mm. An explanation of the calculation of the lifetime can be found above. For a pd-value of 2 mbar $\times$ cm the lifetime of the optics will be 10^8 shots (green line), further lifetime improvement (up to 5 $\times 10^9$ shots, indicated by the red line) will be achieved by a cleaning strategy.

Fast ionic-atomic debris

Measurements of the mitigation of fast ionic-atomic debris by the Ar-gas controlled SFT did not show any results. As shown in section 3.5, the ion signal measured at a distance of 70 cm from the pinch and without any mitigation between the plasma and detector, was only 3 mV large. Moving the detector closer to the pinch, made it impossible to detect the signal of the high-energy ions because first contact of these ions with the cup occurs when the cup signal is still disturbed by the signal induced by the EUV radiation. The presence of a vacuum SFT that is between the source and detector (at 70 cm) made the signal too small to detect. With injection of Ar, which means that there is Ar-gas present in the whole setup, a larger noise signal was observed. This is because the EUV radiation excites the Ar-gas and the Ar-ions hit the detector randomly.

From sputtering experiments performed at Philips Aachen, is has been shown that a *pd*-value of 2 mbar $\times$ cm will be sufficient for a mirror lifetime of 5×10^9 shots. With the use of the Beam Extinction model the suppression rate of the fast ionic-atomic debris for this *pd*-value has been calculated to be equal to a factor of 3000.

Because of the injection of Ar-gas inside the SFT some of the EUV radiation will be absorbed by the gas. Assuming that 2 mbar $\times$ cm will be the amount of Ar-gas inside the SFT, then only a fraction of 7% of the EUV radiation at 13.5 nm is absorbed [27]. The absorption of the EUV radiation by the mitigation devices has to be minimized, meaning that the *pd*-value inside the foil trap has to be as small as possible but large enough to suppress the atomic and ionic debris.

6. Conclusion

The Sn-based EUV source generates not only EUV radiation but also produces debris that damages the optics. This results in a decrease of the EUV reflection and thus a reduction of the available EUV power. The lifetime of a mirror that is in function to collect and redirect the EUV-light, is defined by how long the reflectivity remains within 10% of its maximum value. A shot is defined as one single discharge of the Sn-source.

In general one can distinguish between three types of debris and their effect on the optics:

1. Micro-particles ⇒ Locally non-uniform collector surface coverage
2. Slow atomic-ionic ⇒ Uniform collector surface coverage
3. Fast ionic-atomic ⇒ Collector surface sputtering and implantation

For each type of debris the effect of the impact on the optics is different but the optics result in a deterioration of reflection. The micro-particles will result in a locally non-uniform surface coverage; the slow atomic-ionic debris will result in a uniform surface coverage while the fast ionic-atomic debris results in sputtering of, and implantation into the surface. The goal is to reach a reduction of type of debris such that the optics have a lifetime of 5×10^9.

It has been shown with Scanning Electron Microscopy (SEM) images and software that is able to count the droplets according to their size and that there is a large production of micro-particles, varying in size from 0.1 to 10 μm. The speed of these droplets decreases with increasing size. The smallest particles can reach a speed of 640 m/s.

In a setup using a mitigation device for the droplets and measuring the atomic debris with a Quartz Crystal Microbalance (QCM) it has been found that 50% of the total mass of the debris consists of micro-particles whereas 50% is atomic debris. The amount of slow atomic-ionic debris equals 5×10^{15} atoms/shot in a solid angle of 4π directly at the source. Calculation of the amount of atoms present in the discharge plasma showed that there is still room for reduction of the debris production by the source.
Measuring the fast ionic-atomic debris has been found to be very difficult without an ion energy analyzer that deflects the ions according to their charge and mass. Time of flight analysis of measurements with a faraday cup showed that the ion energies vary from 80 eV to about 4.5 keV.

Different mitigation schemes have been tested and proven to be successful. The feasibility of a *rotating foil trap* in combination with a *stationary foil trap* has been shown with the ASML Sn-source. Particle mitigation experiments were performed with the Philips Sn-source, which has a higher repetition rate. Therefore it is better suited for the experiments. It has been found that with a rotation frequency of 75 Hz. This means that droplets with speeds up to 640 m/s are being stopped and that the coverage of the droplets is being reduced to 10% after 5×10^9 shots.

The concept of a *reflective foil trap*, where the foils are deliberately misaligned with respect to the source, has been tested for EUV reflection and droplet mitigation. It has been shown that coating a Mo-foil with Sn decreases the surface roughness to about 5 nm and increases the reflection coefficient. EUV reflection experiments with different grazing angles of incidence showed a good agreement with the theory and high reflection coefficients under small angles of incidence show promising expectations for development of a reflective foil trap.
An extended point source model has been described to model the transmission of droplets through a static foil trap structure. The model, where the origin of the droplets was fitted to a region of width of 2.5 mm, agreed with the experimental results. This shows that the reflected foil trap is able to mitigate the micro-particles so that it can be used as an alternative for the rotating foil trap.

Finally the suppression of slow atomic-ionic and fast ionic-atomic debris by a *gas controlled stationary foil trap* was calculated using two different models. The suppression of slow atomic-ionic debris was measured with a QCM and a suppression factor of 33 was experimentally observed. With the use of the Anisotropic Diffusion model the pressure of the Ar-gas inside the SFT during this experiment was fitted to be equal to 1.7×10^{-2} mbar.
With the Anisotropic Diffusion model, the lifetime of the optics for a *pd*-value of 2 mbar $\times$ cm has been found to be 10^8 shots. A cleaning strategy will be used to improve the lifetime to 5×10^9 shots. The beam extinction model showed that with a *pd*-value of 2 mbar $\times$ cm the suppression of the fast-ionic debris is about 3000.

References

[1] V. Banine, J.P.Benschop, J.P.Leenders, R.Moors, SPIE Proc 3997, 126, 2000

[2] 3rd International EUVL Symposium, November, 2004, Miyazaki, Japan

[3] V.Banine,R.Moors, *Plasma sources for EUVL exposure tools,* J.Phys.D:Appl.Phys. 37, 3207-3212, 2004

[4] M.Richardson et al., *High conversion efficiency mass-limited Sn-based laser plasma source for EUVL*, J.Vac.Sci. B 22, 785-790, 2004

[5] P.A.C.Jansson et al., *Liquid-tin-jet laser-plasma EUV generation,* Appl.Phys.Lett. 84 (13), 2256-58, 2004

[6] W.Neff et al., *Pinch plasma radiation sources for the Extreme Ultraviolet,* Contr.Plasma Phys. 41, 589-597, 2001

[7] R.Lebert et al., *Preliminary results from key experiments on sources for EUV lithography,* Micr.Electr.Eng. 57-58, 87-92, 2001

[8] E.R. Kieft, *Description of the ASML version of the laser-triggered Sn discharge from ISAN, Troitsk,* Technische Universiteit Eindhoven, The Netherlands, 2003 (unpublished)

[9] E.R.Kieft, J.J.A.M.v.d.Mullen, G.M.W.Kroesen, V.Banine, K.N.Koshelev, *Characterization of a vacuum-arc discharge in tin vapor using time-resolved plasma imaging and extreme ultraviolet spectrometry,* Phys. Rev. E 71, 2005

[10] www.polyus.msk.ru

[11] M.Keidar, J.Fan, I.Boyd, I.I.Beilis, *Vaporization of heated materials into discharge plasmas,* J.Appl.Phys. 89, 3095, (2001)

[12] A.Anders, *Cathodic arcs and high power pulsed magnetron sputtering,* Lawrence Berkeley National Laboratory, University of California, www-ibt.lbl.gov/PAG/2003APS.pdf

[13] E.R.Kieft et al., *Collective Thomson scattering experiments on a tin vapor discharge in the prepinch phase,* Phys. Rev. E 70, 2004

[14] E.R.Kieft et al., *Stark broadening experiments on a vacuum arc discharge in tin vapor,* Phys. Rev. E 70, 2004

[15] E.R.Kieft et al., *Sub-ns Thomson scattering on a vacuum arc discharge in tin vapor,* to be published

[16] V. Ivanov, ISAN, Troitsk, Moscow Region, 142092, Russia

[17] I.I.Beilis, A.Nemirovsky, S.Goldsmith, R.L.Boxman, *Two dimensional thermal model of a refractory anode in a vacuum arc,* IEEE Transaction on plasma science 31, 985-962, (2003)

[18] D.D.DiBitonto, P.T. Eubank, R. Mukund, M.R. Patel, M.A. Barrufet, *Theoretical models of the electrical discharge machining process: I. A simple cathode erosion model,* J.Appl.Phys.66(9), 4095-4103, (1989)

[19] R. Mukund, D.D. DiBitonto, P.T. Eubank, M.R. Patel, M.A. Barrufet, *Theoretical models of the electrical discharge machining process: II. The anode erosion model,* J.Appl.Phys.66(9), 4104-4111, (1989)

[20] H.G.Fan, R. Kovacevic, *A unified model of transport phenomena in gas metal arc welding,* J.Phys.D: Appl.Phys 37, 2531-2544, (2004)

[21] O.Ellegaard, T.Nedelea, J.Schou, H.M. Urbassek, *Plume expansion of a laser-induced plasma studied with the particle-in-cell method,* Appl. Surf. Sc. 197, 229-238, (2002)

[22] A. Bogaerts, Z. Chen, R. Gijbels, A. Vertes, *Laser ablation for analytical sampling:what can we learn from modeling*, Spect.A. 58B, 1867-1893, (2003)

[23] C.V.Budtz-Jorgensen, B.B.Doggett, J.Lunney, *Model for laser ablation plume expansion in gases,* The 7th international conference on laser ablation, Greece (2003)

[24] S.S.Harilal, C.V. Dindhu, M.S.Tillack, F.Najmabadi, A.C.Gaeris, *Plume splitting and sharpening in laser-produced Al plasma,* J.Phys.D: Appl. Phys. 35, 2935-2938, (2002)

[25] L.V. Zhigilei, *Dynamics of the plume formation and parameters of the ejected clusters in short-pulse laser ablation,* J.Appl.Phys. A 76, 339-350, (2003)

[26] S.A. Popov, D.I.Proskurovsky, A.V.Batrakov, *Investigation of the erosion drop fraction for liquid-metal explosive-emission cathodes*, IEEE Transactions on plasma science, 27, 851-857, (1999)

[27] Center for X-ray optics, http://www.cxro.lbl.gov/

[28] For details about the Sn-source of Philips Extreme UV: J. Pankert, "Status of Philips' EUV light source", ASML Tech. Conf., paper [5751-27].

[29] T.Houck, M.Garcia, S. Sampayan, *Faraday cup measurements of the plasma plume produced at an X-ray converter*, Lawrence Livermore National Laboratory, Livermore, California 94550 USA

[30] B. Thestrup et al., *A comparison of the laser plume from Cu and YBCO studied with ion probes*, Appl. Surf. 208-209, 33-38 (2003)

[31] L. Torrisi et al., *Ion and neutral emission from pulsed laser irradiation of metals*, Nucl. Instr. B 184, 327-336 (2001)

[32] Philips Extreme UV, Aachen, Germany

[33] D.Klunder, M.v.Herpen, ID 692557, Philips Research, Eindhoven, The Netherlands

[34] D.klunder, M.v.Herpen, V.Banine, ID41 *Reflectivity enhancement of foil trap for temperature reduction*

[35] D.Klunder, *Testing of debris mitigation by means of a reflective foil trap,* Philips Research, unpublished

[36] I.Classen, L.Bakker, *Monte Carlo simulation of gas dynamics in foil traps*, Nat.Lab Report NL-Rep 7197, Philips Research, 2001

Appendix A: Working principle of a Quartz Crystal Microbalance

A quartz crystal, placed in a water-cooled sensor head, is connected to a Quartz Crystal thickness Monitor. The Quartz Crystal thickness Monitor utilizes the piezoelectric sensitivity of the resonance frequency of the quartz crystal to added mass. The QCM uses this mass sensitivity to control the deposition rate and final thickness of a vacuum deposition. When a voltage is applied across the faces of a properly shaped piezoelectric crystal, the crystal is distorted and changes shape in proportion to the applied voltage. When the frequency of the applied voltage is near the resonance frequency of the crystal, a very sharp electro-mechanical resonance is encountered. When mass is added to the face of a resonating quartz crystal, the frequency of the resonance is reduced. This change in frequency is very repeatable and is precisely understood for specific oscillating modes of quartz. This phenomenon is the basis of a measurement tool that can easily detect the addition of less than an atomic layer of a deposited material.

The change in frequency, $\Delta f = f_q - f_c$, of a quartz crystal with coated and uncoated frequencies, f_c and f_q respectively is related to the change in mass from the added material, M_c as follows:

$$\frac{M_c}{M_q} = \frac{\Delta f}{f_q} \quad \text{(A.1)}$$

where M_q is the mass of the uncoated quartz crystal. We that M_c can be written as

$$M_c = T_c \cdot A \cdot \rho_c \quad \text{(A.2)}$$

where T_c is the thickness of the coating, ρ_c is the density of the deposited material and A is the exposed surface. M_q can be expressed as follows

$$M_q = T_q \cdot A \cdot \rho_q \quad \text{(A.3)}$$

where T_q is the thickness of the quartz crystal and ρ_q the density. T_q can be rewritten as

$$T_q = \frac{N_q}{f_q} \quad \text{(A.4)}$$

with N_q the frequency constant for an AT cut quartz crystal, which is equal to 1.668×10^5 Hz × cm. Substitutions of formula A.2, A.3 and A.4 into A.1 lead to the equation that is used to calculate the film thickness

$$T_c = \frac{N_q \rho_q}{\rho_c f_q^2} \Delta f \quad \text{(A.5)}$$

Appendix B: Transmission of the Nb-filter

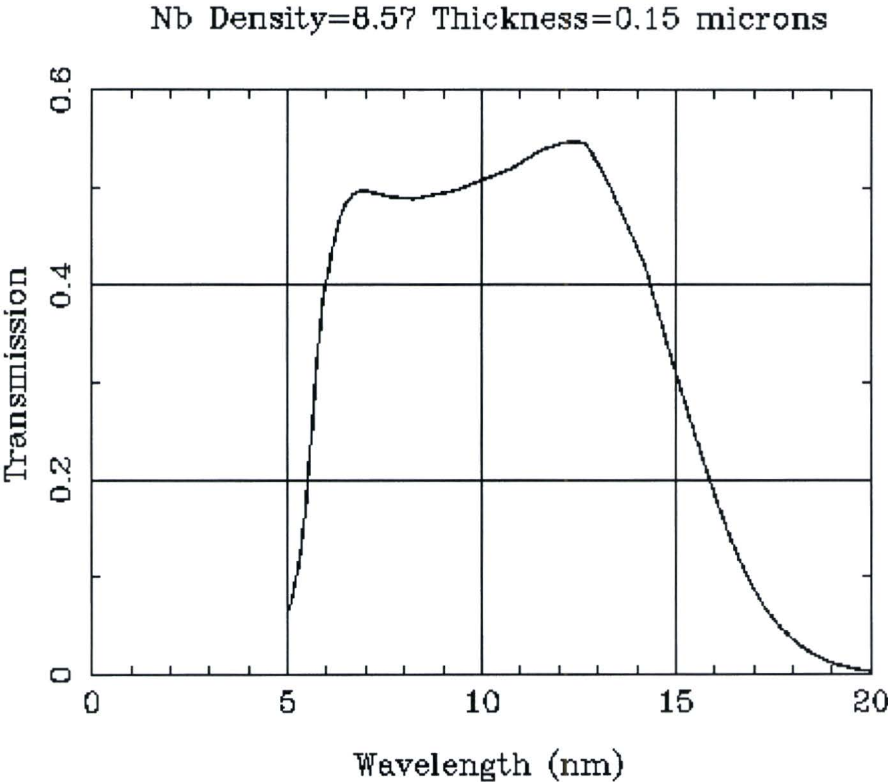

[27]

Appendix C: Transmission of droplets through the foil trap

The transmission is calculated using a 1 D model where the foils and the traces of the droplets from the pinch towards the foils are in a single plane. The pinch is considered to be a point source. The foils are assumed thin relative to the mutual distance b between the foils. A foil trap of length L is placed at a distance Z_{in} from the pinch with the central pair of foils (slit nr. 0) centered around the optical axis, as shown in figure C1. The transmission of the foil trap is symmetrical around slit 0 so it sufficient to find expressions for the transmission of slit 0 and slit n with n positive. It is clearly seen that the transmission for slit 0 is given by

$$T_0 = \frac{2\beta_0}{2\gamma_0} \tag{C.1}$$

$$T_0 = \frac{\arctan\left(\dfrac{b/2}{Z_{in}+L}\right)}{\arctan\left(\dfrac{b/2}{Z_{in}}\right)} \tag{C.2}$$

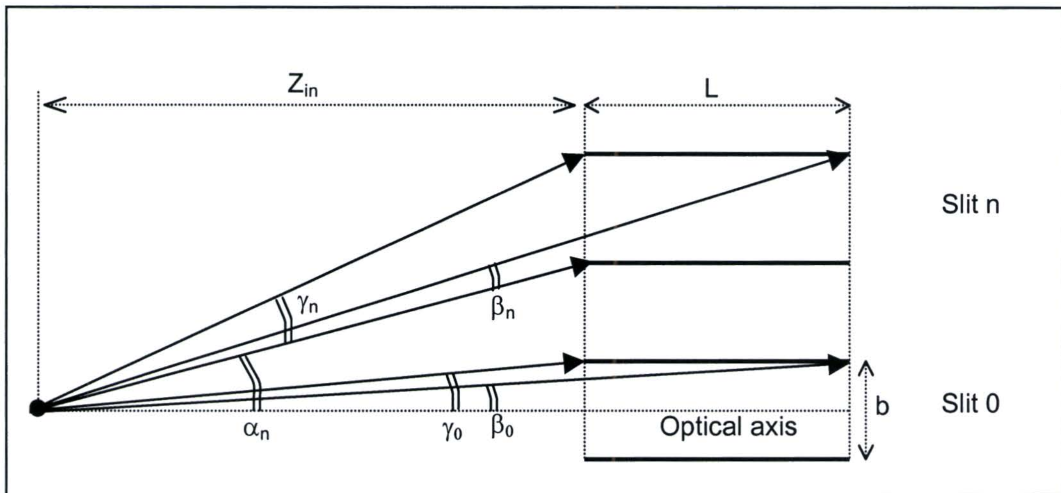

Figure C1: Schematic of the 1 D model used to estimate the transmission of the foil trap for the droplets. The foil trap of length L is placed at a distance Z_{in} from the pinch. The foil spacing is equal to b.

For slit n the position of the first foil is at an angle α_n and the next foil at an angle $(\alpha_n + \gamma_n)$ with respect to the optical axis. The angle for which droplet transmission occurs, is indicated with β_n. The transmission of droplets through a slit happens as long as $\beta_n > 0$ and is given by

$$T_n = \frac{\beta_n}{\gamma_n} \tag{C.3}$$

Now expressions for β_n and γ_n in function of the setup parameters have to be found. β_n can be rewritten as

$$\beta_n = (\alpha_n + \beta_n) - \alpha_n \tag{C.4}$$

with

$$\alpha_n = \arctan\left(\frac{b(|n| - 1/2)}{Z_{in}}\right) \tag{C.5}$$

$$\alpha_n + \beta_n = \arctan\left(\frac{b(|n| + 1/2)}{Z_{in} + L}\right) \tag{C.6}$$

Filling formula C.6 and C.5 into C.4 gives the expression for β_n

$$\beta_n = \arctan\left(\frac{b(|n| + 1/2)}{Z_{in} + L}\right) - \arctan\left(\frac{b(|n| - 1/2)}{Z_{in}}\right) \tag{C.7}$$

γ_n can be rewritten as

$$\gamma_n = (\alpha_n + \gamma_n) - \alpha_n \tag{C.8}$$

with

$$\alpha_n + \gamma_n = \arctan\left(\frac{b(|n| + 1/2)}{Z_{in}}\right) \tag{C.9}$$

Filling formula C.9 and C.5 into C.8 gives us an expression for γ_n

$$\gamma_n = \arctan\left(\frac{b(|n| + 1/2)}{Z_{in}}\right) - \arctan\left(\frac{b(|n| - 1/2)}{Z_{in}}\right) \tag{C.10}$$

This formula together with C.7 and C.3 gives the transmission for slit n, with $n \neq 0$

$$T_n = \frac{\arctan\left(\frac{b\left(|n|+1/2\right)}{Z_{in}+L}\right) - \arctan\left(\frac{b\left(|n|-1/2\right)}{Z_{in}}\right)}{\arctan\left(\frac{b\left(|n|+1/2\right)}{Z_{in}}\right) - \arctan\left(\frac{b\left(|n|-1/2\right)}{Z_{in}}\right)} \quad \text{(C.11)}$$